



# CHORUS

This is the accepted manuscript made available via CHORUS. The article has been published as:

## Phenomenological model for light-projectile breakup

C. Kalbach

Phys. Rev. C **95**, 014606 — Published 17 January 2017

DOI: [10.1103/PhysRevC.95.014606](https://doi.org/10.1103/PhysRevC.95.014606)

# Phenomenological Model for Light-Projectile Breakup

C. Kalbach

*Physics Department, Duke University, Durham North Carolina 27708-0305, USA*

(Dated: 27 July 2016)

**Background:** Projectile breakup can make a large contribution to reactions induced by projectiles with mass numbers 2, 3, and 4, yet there is no global model for it and no clear agreement on the details of the reaction mechanism.

**Purpose:** This project aims to develop a phenomenological model for light-projectile breakup that can guide the development of detailed theories and provide a useful tool for applied calculations.

**Method:** An extensive database of double-differential cross sections for the breakup of deuterons,  $^3\text{He}$  ions, and  $\alpha$  particles was assembled from the literature and analyzed in a consistent way.

**Results:** Global systematics for the centroid energies, peak widths, and angular distributions of the breakup peaks have been extracted from the data. The dominant mechanism appears to be absorptive breakup, where the unobserved projectile fragment fuses with the target nucleus during the initial interaction. The global target-mass-number and incident-energy dependences of the absorptive breakup cross section have also been determined, along with channel-specific normalization constants.

**Conclusions:** Results from the model generally agree with the original data after subtraction of a reasonable underlying continuum. Absorptive breakup can account for as much as 50 to 60% of the total reaction cross section.

## I. INTRODUCTION

When nuclear reactions are induced by projectiles with mass numbers  $A_a = 2, 3$ , or 4 and incident energies of 15 to 150 MeV (where preequilibrium effects are important), a global description of light-particle emission needs to include projectile breakup along with direct nucleon transfer, preequilibrium emission, and particle evaporation. The other mechanisms are already typically included in comprehensive statistical model codes, while projectile breakup has been the missing piece. Projectile breakup in this work is defined as the emission of a projectile fragment with a fairly narrow energy distribution peaked at an emission energy corresponding approximately to the projectile velocity. These fragments are also emitted with an angular distribution that is more strongly focused toward forward angles than the underlying cross section.

The effect of projectile breakup on reaction calculations is first to reduce the amount of the total reaction cross section going into the preequilibrium and compound nucleus models. In addition, when an undetected fragment interacts with the target nucleus to form a composite system, that system will then undergo energy equilibration. Particle emission during and after such equilibration must also be considered. Inclusion of these effects will enable a better assessment of the initial particle-hole configuration in the exciton statistical preequilibrium model. The importance of projectile breakup is most obvious for incident deuterons because of their low internal binding energy, but the breakup mechanism also makes significant contributions for reactions induced by  $^3\text{He}$  ions [1, 2] and, at sufficiently high incident energies, by  $\alpha$  particles [3, 4].

Beginning with the well-known Serber model for deuteron breakup [5], various theoretical models for projectile breakup have been developed (see e.g. Refs. [1, 3, 6–11]). However, they must typically make assumptions about details of the reaction mechanism that are

not well understood and that become more complex as the mass of the projectile—and therefore the number of possible breakup channels—increases. Furthermore, the assumptions made and even the definition of projectile breakup vary from one model to another. The nature and importance of projectile breakup are discussed further in Sects. III and IX, respectively. More recently, with the advent of radioactive ion beams, the concept of projectile breakup has been extended to much heavier and more complex projectiles (for a review see, for instance, Ref. [12]), but that is outside the scope of the present work.

Light-projectile breakup is also of growing concern for practical applications. The International Atomic Energy Agency recently completed a Coordinated Research Project (CRP) to update the Fusion Energy Nuclear Data Library (FENDL) [13]. One of the important goals was the inclusion of deuteron-induced reactions. This relied heavily on reaction model calculations, and the inclusion of a projectile-breakup model was a necessary part of the project. An earlier version of the present model is described in the final report for the FENDL-3 CRP [13].

Given the importance of light-projectile breakup, both from a basic physics perspective and for energy applications, and given the lack of a definitive, simple, global model for it, a phenomenological breakup model has been developed. It is designed for inclusion in comprehensive reaction model codes, and an earlier version of the model for deuteron breakup already exists in TALYS [14]. Once the new model is implemented, it will facilitate the calculation of both excitation functions (needed for medical isotope production and for hardware irradiation estimates at fusion-energy facilities) and double-differential cross sections (needed for radiation shielding calculations). Such applications require an accurate description of all contributing reaction mechanisms. The relative importance of those mechanisms will vary depending on the incident energy, projectile, target nucleus, and other ex-

TABLE I: Literature data used in developing the projectile breakup model.

Proj.	$E_{inc}$ (MeV)	Targets	Ejectile	Angles	Ref.
d	14.8	Al, Cu, Zr, Cd, Pt	p	12°–85°	[6]
	14.8	11 others	p	30°	[6]
	15.0	$^{62}\text{Ni}$ , Ta	p	23°–120°	[15]
	25.5	Al, $^{62}\text{Ni}$ , Nb, $^{119}\text{Sn}$ , Ta	p	20°–120°	[7]
	27.5	$^{57}\text{Fe}$ , $^{116}\text{Sn}$	p	20°–90°	[16]
	56	Al, $^{58}\text{Ni}$ , $^{90}\text{Zr}$ , $^{118}\text{Sn}$ , Bi	p	9.5°–30°	[8]
	56	9 others	p	9.5°	[8]
	70	$^{90}\text{Zr}$ , $^{208}\text{Pb}$ , $^{232}\text{Th}$	p	20°–90°	[17]
	80	Al, $^{58}\text{Ni}$	p	20°–90°	[17]
	$^3\text{He}$	70, 90, 110	$^{90}\text{Zr}$	d	13°–30°
70		6 others	d	13°	[1]
90		11 others	d	13°	[1]
70, 90		$^{90}\text{Zr}$	p	13°–40°	[1]
130		Al, Co, Nb, Au	d	7.5°–21°	[2]
$\alpha$	80	Al, $^{58}\text{Ni}$ , $^{90}\text{Zr}$	p,d	6°–26°	[4]
	80	Al	t, $^3\text{He}$	6°–26°	[4]
	140	Bi	$^3\text{He}$	13°–20°	[3]
	160	Al, $^{58}\text{Ni}$ , $^{90}\text{Zr}$ , Bi	p,d,t, $^3\text{He}$	6°–26°	[4]

perimental variables, and all the mechanisms should be included in a comprehensive code.

## II. DATABASE

The current model was developed using data for deuteron,  $^3\text{He}$ -ion, and  $\alpha$ -particle breakup. This yields a more robust and global model than one developed for a single projectile type, because it uncovers the dependence of the breakup reaction on the energy required to separate the projectile into its constituent fragments and on the relative sizes of the projectile and detected fragment. Double-differential cross section measurements were employed because they allow the breakup cross section to be isolated from other contributions using its experimental signature so that both the energy and angular distributions of the emitted breakup fragments can be studied.

Continuum energy spectra measured at a variety of forward angles for a given reaction have been collected from the literature. All of the detected fragments are charged particles, so it is assumed that neutron fragments follow generally the same systematics as proton fragments, except, of course, that there will be no Coulomb barrier in the exit channel. The data used [1–4, 6–8, 15–17] are summarized in Table I. Other data at lower incident energies are available for  $^3\text{He}$  and  $\alpha$ -particle projectiles, but the breakup peaks, when present, are not distinct enough to be used in this study.

In order to develop a model for projectile breakup, the breakup peak must be differentiated from the underlying continuum, which is typically the usual preequilibrium cross section. A continuum “background” was

drawn underneath the obvious breakup peak for all of the spectra analyzed and represents the greatest source of uncertainty in the present work. Even the assignment of uncertainties is subjective. Fortunately, both the peak energies and peak widths appear to be largely independent of the emission angle, so data from more than one angle can be used to reduce uncertainties. All analyses are carried out in the laboratory system because of the spectator nature of the detected breakup fragments. Special problems in individual data sets are discussed where they become relevant.

## III. CENTROID ENERGIES

The easiest property of projectile breakup to characterize is the peak energy, and the simplest estimate is that of a fragment moving at the projectile’s velocity. This would give a peak centered at an energy  $E_0 = E_{inc} A_b/A_a$ , where  $A_a$  and  $A_b$  are the mass numbers of the projectile and detected fragment, respectively, and  $E_{inc}$  is the projectile energy in the laboratory system. The actual peak energy will be shifted from this value by Coulomb deceleration in the entrance channel and by Coulomb acceleration in the exit channel, as noted in Ref. [1]. In addition, when both projectile fragments continue moving forward at roughly the initial velocity, the need to supply the projectile’s dissociation energy will lower the peak energy. This would be seen most easily in  $\alpha$ -particle breakup because it takes around 20 MeV to break an  $\alpha$  particle into two fragments. The observed peak energies for  $\alpha$ -particle breakup in the current database show no indication of this lowering, so this is

not the dominant reaction mechanism.

### A. Empirical relation

The observed peak energies have been assumed to follow the relation

$$E_0 = \frac{A_b}{A_a} (E_{\text{inc}} - C_a) + C_b, \quad (1)$$

where  $C_a$  and  $C_b$  are the Coulomb barriers in the entrance and exit channels, respectively. The barrier  $C_a$  is given by

$$C_a = 1.44 \text{ MeV fm } Z_a Z_A / D_0, \quad (2)$$

where  $Z_a$  and  $Z_A$  are the atomic numbers of the projectile and target, respectively. A similar expression applies for  $C_b$ . Here  $D_0$  is the effective target-projectile separation at the point of interaction.

Using the experimental peak positions for the heaviest targets (those with the largest Coulomb barriers), estimates of the Coulomb shifts in the peak positions have been used to extract values for  $D_0$ . These results have been studied assuming

$$D_0 = r_0 A_A^{1/3} + 1.2 \text{ fm}, \quad (3)$$

where  $r_0$  is an effective radius parameter that depends only on the incident energy and where the constant 1.2 fm accounts for the size of the projectile. Here  $A_A$  is the target mass number. Values of  $r_0$  were extracted and are shown in Fig. 1. The values for the three projectile types seem to follow a common trend described by the formula

$$r_0 = 1.2 \text{ fm} + \frac{5 \text{ fm}}{1 + \exp(E_{\text{inc}}/30 \text{ MeV})}. \quad (4)$$

Equation (4) is assumed to apply for all targets.

The systematic peak energies for  $(d,p)$ ,  $({}^3\text{He},d)$ , and  $({}^3\text{He},p)$  breakup obtained from Eqs. (1–4) are shown along with the experimental values in Fig. 2. Figure 3 shows the same quantities for  $\alpha$ -particle breakup. Overall, the systematics agree with the peak energies across the range of target masses. For  $\alpha$ -particle breakup, there is a tendency for the model to underestimate the peak energies in the  $(\alpha,d)$  channel at both incident energies and in the  $(\alpha,t)$  channel at 160 MeV. However, except for  $(\alpha,d)$  at 80 MeV, the results generally agree within the estimated uncertainties.

The  $(\alpha,xd)$  spectra from 160 MeV show a second peak at the energy corresponding to the  $(\alpha,p)$  breakup peak and with the same width and angular distribution as the  $(\alpha,p)$  peak. A corresponding but much weaker peak is just barely evident in the data at 80 MeV. These “extra” peaks were noted in the original article [4] and are discussed in Sect. VI.

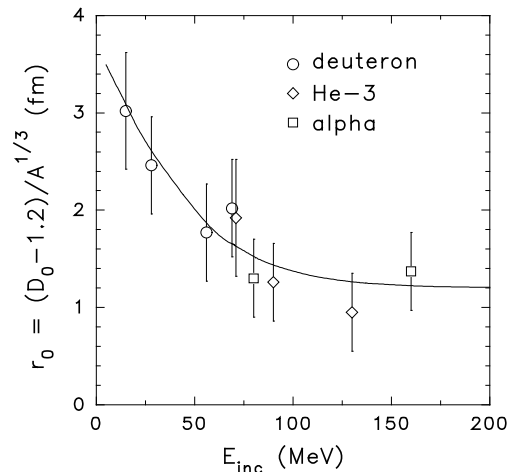


FIG. 1: Effective radius parameter for projectile breakup. The points show the values deduced from the observed Coulomb shifts of the breakup peaks for the indicated projectiles and the heaviest available target. The curve is obtained from Eq. (4).

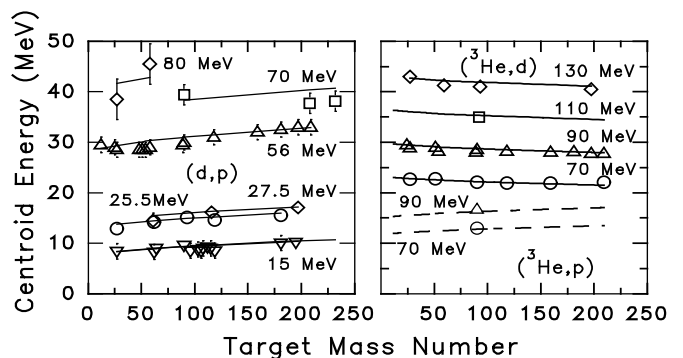


FIG. 2: Peak energies for  $(d,p)$ ,  $({}^3\text{He},d)$ , and  $({}^3\text{He},p)$  breakup. The points show the values extracted from the data at the indicated incident energies; the lines are from Eqs. (1–4).

### B. Breakup mechanisms

In the present analysis, the peak energies do not seem to be lowered by supplying part of the projectile’s dissociation energy, suggesting that the dominant mechanism involves the emission of only one fragment and that the projectile’s dissociation energy is supplied by the strong interaction of the other fragment with the target. This is consistent with the results of coincidence measurements on the breakup of 140 MeV  $\alpha$  particles [18]. That work differentiates two mechanisms in which both fragments are emitted and that together account for only a few percent of the total breakup cross section. In “final state breakup,” the projectile is first inelastically scattered to an excited state and then breaks up as it moves out of the interaction zone. In “quasi-free breakup,” it dissociates

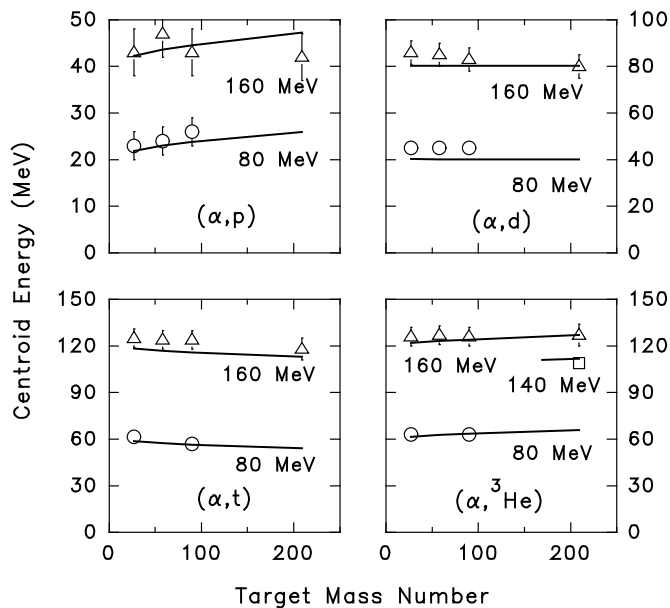


FIG. 3: Peak energies for  $(\alpha, p)$ ,  $(\alpha, d)$ ,  $(\alpha, t)$ , and  $(\alpha, {}^3\text{He})$  breakup at the indicated incident energies. The points and curves have the same significance as in Fig. 2.

during the initial interaction with the target, leaving the target in its ground state or a low-lying excited state. By far the dominant mechanism is what they term “absorptive breakup,” in which part of the projectile fuses with the target nucleus while the remaining fragment is largely a spectator. The term absorptive breakup is therefore used to refer to the dominant breakup peaks analyzed here.

For incident deuterons, DWBA breakup calculations for deuteron energies between 10 and 30 MeV have been performed in terms of “elastic breakup” and “breakup-fusion” [19]. The latter mechanism is described as a sequential process in which elastic breakup (leaving the target in its ground state) is followed by fusion of one of the fragments with the target nucleus. The authors find breakup-fusion to be dominant. However, this mechanism would imply that the projectile’s dissociation energy would always lower the energy of an observed fragment. Such a reduction is difficult to observe in deuteron breakup because the deuteron’s internal binding energy is only 2.2 MeV, but the consistency of the present results for  $d$ ,  ${}^3\text{He}$ , and  $\alpha$ -particle breakup indicates a contradiction with this assumption.

Other DWBA calculations for deuteron breakup in the same energy domain [15] differentiate between what they call “elastic breakup” and “inelastic breakup,” where they, like the authors of Ref. [18], discuss two different mechanisms for the former. Inelastic breakup, where there is a strong interaction with the target, is found to be dominant, but their calculated component for it seems also to include stripping reactions to unbound states in the final nucleus.

More recently, still other DWBA calculations [11] for incident deuterons of 25.5 and 56 MeV (the same data analyzed here) also include two elastic breakup components, along with what they term “non-elastic” breakup, which includes direct stripping. The authors find a contribution from elastic breakup that is comparable to their non-elastic component at the most forward angles and is thus a larger part of the total breakup component than in other estimates.

Absorptive breakup seems to have much in common with direct stripping, since both cases involve a direct reaction in which one fragment of the projectile is absorbed by the target while the remaining fragment is emitted. However, the experimental signatures of the two mechanisms are different. Thus, while it seems to be natural in many more-formal theoretical approaches to treat the two reaction mechanisms together, the same is not true for phenomenological continuum models. The energy spectrum for particles emitted in direct stripping is broad, while the spectrum for projectile breakup is sharply peaked near the projectile velocity. The general angular distribution systematics [20] account for all of the continuum cross section (including direct stripping) except for an excess at very forward-angles, where the excess cross section has an angular distribution that falls off more rapidly with increasing angle and an energy spectrum peaked near the projectile velocity. The observed fragment is therefore more of a spectator in light-projectile breakup. Direct stripping and its counterpart of direct pickup are typically already treated in general statistical model codes, while projectile breakup as defined here has been the missing mechanism.

## IV. PEAK SHAPES AND WIDTHS

### A. Base systematics

The breakup peaks are assumed to have a Gaussian shape so that the normalized energy distribution is

$$P_E(E) = \frac{1}{\sqrt{2\pi}w} \exp\left[-\frac{(E - E_0)^2}{2w^2}\right], \quad (5)$$

where  $w$  is the peak width, and  $E$  is the laboratory energy of the observed breakup fragment.

The full width at half maximum (FWHM) of the breakup peaks is  $F = 2.35w$ . Values for  $F$  estimated from the data are generally independent of emission angle and only weakly dependent on target mass number. A workable empirical formula is

$$F = 62 \text{ MeV} \left[ 1 - \frac{1}{\exp(E_{\text{inc}}/173 \text{ MeV})} \right] \times \left[ 1 - \frac{A}{155 \text{ MeV}^{-2}(S_{a,b})^2} \right] - 3\Theta(A_a - A_b - 1.5), \quad (6)$$

where  $S_{a,b}$  is the energy required to separate the projectile  $a$  into the observed fragment  $b$  and its complement, and  $\Theta$  is the Heaviside step function, which is zero for a negative argument and one for a positive argument. The last term in Eq. (6) lowers the peak width for  $({}^3\text{He},p)$ ,  $(\alpha,p)$  and  $(\alpha,d)$  breakup relative to the channels where only a single nucleon is absorbed by the target. This difference between channels with  $A_b = A_a - 1$  and those with  $A_b < A_a - 1$  was unexpected but appears again in the angular distribution systematics discussed in Sect. V. A comparison of widths obtained from Eq. (6) with the experimental values for  $d$  and  ${}^3\text{He}$  breakup is shown in Fig. 4. Results for  $\alpha$ -particle breakup are in Fig. 5.

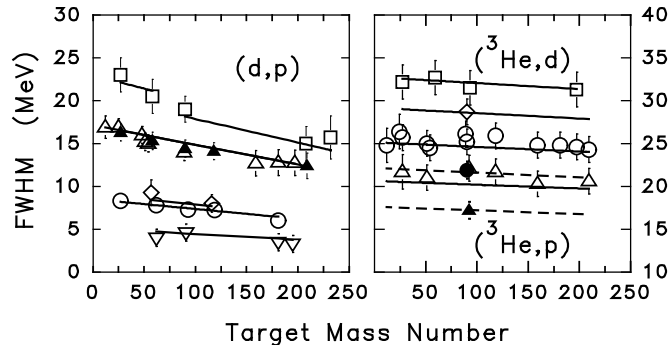


FIG. 4: FWHM for  $d$  and  ${}^3\text{He}$  breakup peaks. The points show the experimental values, and the lines are obtained from Eq. (6). The incident energies for  $(d,p)$  breakup are (top to bottom) 80, 70, 56, 27.5, 25.5, and 14.8 MeV. At 56 MeV, the solid points include data from multiple angles, while the open points are from 30-deg spectra. The incident energies for  $({}^3\text{He},d)$  breakup (open points) are 130, 110, 90, and 70 MeV. The  $({}^3\text{He},p)$  results at 90 and 70 MeV are given by the solid points and the dashed curves.

Agreement between the systematic and measured peak widths is good except for  $(\alpha,{}^3\text{He})$ , where the discrepancies are due to the kinematic limit on the fragment energy. In fact, the peak shapes, widths, and even their positions can be modified by either the Coulomb barrier or the maximum-energy cutoff in the spectrum due to energy conservation. These effects were not obvious in deuteron or  ${}^3\text{He}$  breakup, but the maximum-energy cutoff plays a role in  $(\alpha,t)$  and  $(\alpha,{}^3\text{He})$  breakup. Both effects have been included in the model.

### B. Modifications from the Maximum-Energy Cutoff and the Coulomb Barrier

The unusually narrow  $(\alpha,t)$  and  $(\alpha,{}^3\text{He})$  breakup peaks are also asymmetric, with the higher emission energy side narrowed due to the kinematic limit on the energy of the observed fragment. This effect can be included in the model by leaving the peak in its normal position and using different widths for the two sides of the Gaussian

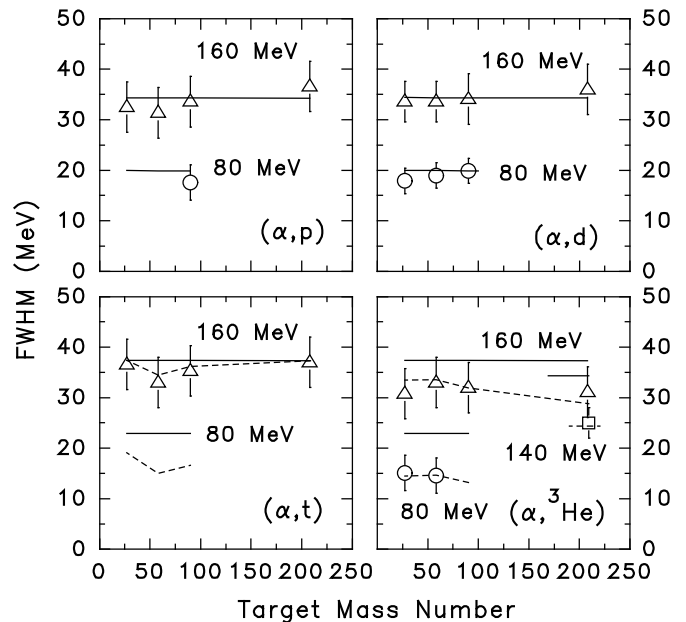


FIG. 5: FWHM for  $\alpha$ -particle breakup peaks. The points show the experimental values, the solid and dashed lines are obtained from Eqs. (6) and (7), respectively. The  $(\alpha,{}^3\text{He})$  channel has an intermediate result for a bismuth target at 140 MeV. The data for  $(\alpha,t)$  breakup at 80 MeV did not allow reliable widths to be extracted.

distribution. If  $E_{\text{max}}$  is the maximum kinematically allowed laboratory energy of the emitted fragment at the emission angle where the breakup peak has its maximum intensity (defined in Sect. V in terms of the angular barrier), and if  $H = F/2$  is the half width at half maximum from the base systematics, then the full width at half maximum becomes

$$F_{\text{eff}} = H + \min[H, 0.6(E_{\text{max}} - E_0)], \quad (7)$$

where the factor of 0.6 is an empirical estimate. The resulting FWHM values for the current data set are different from the base systematics only for  $(\alpha,t)$  and  $(\alpha,{}^3\text{He})$  breakup, and the reduced values from Eq. (7) are shown as dashed curves in Fig. 5. Thus including a known piece of physics with one free global parameter consistently improves agreement with experiment.

In the more extreme case where  $E_{\text{max}} < E_0$ ,  $E_{\text{max}}$  becomes the new peak energy. This can occur, for instance, in  $(\alpha,t)$  and  $(\alpha,{}^3\text{He})$  breakup at incident energies below about 40 MeV. Therefore two additional ranges of  $E_{\text{max}}$  are defined. The peak shape for each range is characterized by its half widths at half maximum,  $H_-$  and  $H_+$ , for the half Gaussians lying below and above the peak energy  $E_{\text{pk}}$ , respectively, so that the effective FWHM becomes

$$F_{\text{eff}} = H_- + H_+. \quad (8)$$

The full prescription is summarized in Table II, where the peak energy is  $E_{\text{pk}} = \min(E_0, E_{\text{max}})$ .

TABLE II: Equations for the half widths at half maximum for the breakup-fragment energy distribution.

Range of $E_{\max}$	$H_-$	$H_+$	$E_{\text{pk}}$
$E_0 + 1.67H \leq E_{\max}$	$H$	$H$	$E_0$
$E_0 \leq E_{\max} < E_0 + 1.67H$	$H$	$0.6(E_{\max} - E_0)$	$E_0$
$E_0 - 1.67H \leq E_{\max} < E_0$	$H - 0.6(E_0 - E_{\max})$	0	$E_{\max}$
$E_{\max} < E_0 - 1.67H$	0	0	

Finally, there is the question of the exit-channel Coulomb barrier. If it is high enough to distort the peak shape, the equation for the Gaussian should be multiplied by a barrier penetrability factor. Using the simple form for a parabolic barrier centered at an energy  $C_b$ , a reasonable barrier width was chosen by looking at systematics of total reaction cross sections. The resulting formula for the barrier penetrability is

$$T_E(E) = \left[ 1 + \exp\left(\frac{C_b - E}{C_b/3}\right) \right]^{-1}, \quad (9)$$

where  $E$  is again the laboratory energy of the observed fragment. The penetrability factor was not included in the data analysis, nor did it seem to be needed, but it is included in the model and in the comparisons with data.

The resulting energy distribution for absorptive breakup is

$$P_E(E) = \begin{cases} \frac{1}{\sqrt{2\pi w}} \exp\left[-\frac{(E-E_{\text{pk}})^2}{2(2w_i)^2}\right] T_E(E) & \text{for } w_i > 0 \\ 0 & \text{for } w_i \leq 0 \end{cases}, \quad (10)$$

where

$$w = w_+ + w_- = \frac{F_{\text{eff}}}{2.35}, \quad (11)$$

$$w_+ = \frac{H_+}{2.35} = \frac{1}{2.35} \max\{0, \min[H, 0.6(E_{\max} - E_0)]\}, \quad (12)$$

$$w_- = \frac{H_-}{2.35} = \frac{1}{2.35} \max(0, \{H - \max[0, 0.6(E_0 - E_{\max})]\}), \quad (13)$$

$$w_i = \begin{cases} w_- & \text{for } E \leq E_{\text{pk}} \\ w_+ & \text{for } E > E_{\text{pk}} \end{cases}. \quad (14)$$

In the base case, with no peak distortion,  $P_E(E)$  is a normalized energy distribution. When the distribution is distorted by the kinematic limit on the breakup fragment's energy, the use of  $w = w_+ + w_-$  in the pre-exponential of Eq. (10) preserves the normalization for peaks with a finite width. However, when the Coulomb barrier penetrability lowers the breakup cross section,  $P_E(E)$  is no longer normalized.

## V. ANGULAR DISTRIBUTIONS AND A-DEPENDENCE OF THE BREAKUP CROSS SECTION

The database for describing the breakup-fragment angular distributions is more limited because it is necessary to have data at multiple angles. Thus the derived systematics are more tentative.

### A. Target Mass Dependence

For a given breakup channel and incident energy, the data show that at each emission angle the breakup cross section is generally proportional to  $(D_0)^2$ , where  $D_0$  is again the separation distance between target and projectile at the point of interaction. Thus the data from multiple targets can be divided by  $(D_0)^2$  and plotted as a function of the laboratory emission angle in order to study the average angular distribution systematics.

The target-mass dependences of the breakup cross section found in many of the data references vary between  $A^{1/3}$  and  $A^{2/3}$ , in one case tending toward  $A$ , depending on what kind of background (if any) was subtracted and on whether the data or normalized model calculations were integrated. This underscores the difficulty in separating the breakup peaks from the underlying continua. The significance of the present  $(D_0)^2$  dependence is that it was obtained using a consistent continuum correction across a broad database.

The spectator nature of the detected fragment in absorptive breakup would lead one to expect light-projectile breakup to be a peripheral process and therefore characterized by a  $D_0$ , rather than a  $(D_0)^2$ , dependence, but the latter is clearly indicated by the data. This point is illustrated for  $(d,p)$  breakup at 56 MeV where the theoretical calculations of Ref. [11] produce an  $A^{1/3}$  dependence of the breakup cross section compared to the  $(A^{1/3} + 0.8)^2$  dependence deduced from the data [8] by the original authors

### B. Base Angular Distribution Systematics

With the exception of  $(d,p)$  breakup for targets with  $A \geq 90$  at an incident energy of around 15 MeV, the data generally display an angular distribution that is a negative exponential in the emission angle  $\theta$ , though there

is also a small deviation for  $^{197}\text{Au}(^3\text{He},d)$  at 130 MeV. The general behavior is shown for the 56 MeV ( $d,p$ ) data in Fig. 6. Here the angle-differential cross section has been estimated from the empirical peak height (after subtraction of an underlying continuum) and the systematic FWHM. Where there is a deviation from the exponential dependence, it is typically for the lightest target(s) at the most backward angle(s), as seen in Fig. 6. This is where the breakup cross section is smallest and hardest to estimate. Therefore the discrepancies are often within generous but reasonable error estimates. The most extreme case is ( $^3\text{He},d$ ) breakup at 130 MeV for the aluminum and cobalt targets. It is discussed further in Sect. VIII C, where those data are compared with model calculations.

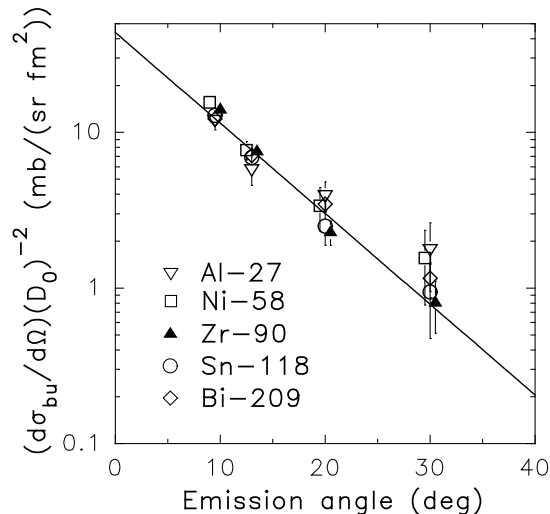


FIG. 6: Normalized angular distributions for ( $d,p$ ) breakup at 56 MeV. The points show the experimental breakup cross sections divided by  $(D_0)^2$  as a function of laboratory angle, while the line shows the best-fit exponential.

The points in Fig. 6 and similar plots were fit with the exponential  $Ke^{-a_{bu}\theta}$ , where  $K$  and  $a_{bu}$  were the fitting parameters. The result for ( $d,p$ ) breakup at 56 MeV is also shown in Fig. 6. The systematics of the angular distribution slope parameter  $a_{bu}$  were then studied, and, as with the peak widths, a difference was found between the breakup channels with  $A_b = A_a - 1$  and those with  $A_b < A_a - 1$ . In the latter case,  $a_{bu}$  appears to be independent of the incident energy and peak position. The results for  $A_b = A_a - 1$  can be described using either the incident energy or the peak energy. The peak energy gives a slightly better fit and is more consistent with the systematics for the angular distributions of the underlying continuum, for which the primary dependence is on the emission energy.

The empirical average slope parameters  $a_{bu}$  are shown in Fig. 7 as a function of  $\langle E_0 \rangle$ , the calculated peak energy averaged over the different targets for that breakup channel and incident energy. The error bars in the figure reflect only the uncertainty in the slope values assigned

by the fitting program.

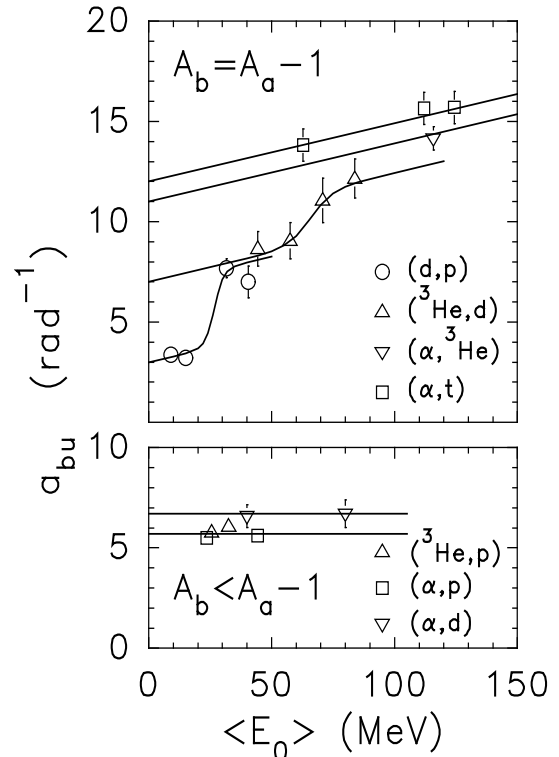


FIG. 7: Empirical values for  $a_{bu}$ , the slope parameter of the breakup angular distributions, shown as a function of the average peak energy of the available targets. The lines show the systematics given by Eq. (15).

For  $A_b = A_a - 1$ , a linear dependence of  $a_{bu}$  on the peak energy did not prove adequate, so a mathematical form with a rise at an energy proportional to  $S_{a,b}$  was adopted. The resulting  $a_{bu}$  values in  $\text{rad}^{-1}$  are

$$a_{bu} = 4A_b + Z_b - 2 + (0.029 \text{ MeV}^{-1})E_0 + \frac{7.6}{A_a} [1 + \exp\{(12S_{a,b} - E_0)/0.84S_{a,b}\}]^{-1} \quad (15a)$$

for  $A_b = A_a - 1$

$$a_{bu} = 4.7 + A_b \quad \text{for } A_b < A_a - 1, \quad (15b)$$

The first three terms in Eq. (15a) give the  $y$ -intercepts of the curves in the upper part of the figure; the fourth term gives the underlying slope, determined mainly from the ( $\alpha,^3\text{He}$ ) data; and the last term describes the rise in  $a_{bu}$  occurring near a peak energy of  $12S_{a,b}$ . Values obtained from Eq. 15 are shown in Fig. 7 and account well for the experimental values.

### C. Coulomb Dip at Forward Angles

For ( $d,p$ ) breakup at around 15 MeV, the breakup peaks for the heavier targets are low at forward angles, then increase with angle until they bend over and begin

to follow the normal exponential falloff. The size of the dip at forward angles appears to be correlated with the size of the entrance channel Coulomb barrier relative to the incident energy, implying that it should be the same for all breakup channels for a given target, projectile, and incident energy. The dip has been parameterized as an angular penetrability factor multiplying the basic exponential dependence. Thus the emission probability per unit solid angle at a particular angle  $\theta$  becomes

$$P_{\theta}(\theta) = \frac{(a_{\text{bu}})^2 + 1}{2\pi} e^{-a_{\text{bu}}\theta} T_{\theta}(\theta), \quad (16)$$

$$T_{\theta}(\theta) = \left[ 1 + \exp\left(\frac{\theta_0 - \theta}{w_{\theta}}\right) \right]^{-1}. \quad (17)$$

The factor  $[(a_{\text{bu}})^2 + 1]/2\pi$  normalizes the probability function in the absence of a forward-angle dip if a factor of  $(e^{-a_{\text{bu}}\pi} + 1)$  in the denominator of the normalization factor is neglected. The dip reduces the breakup cross section. Here  $\theta_0$  characterizes the angular ‘‘barrier,’’ and  $w_{\theta}$  determines its width. Unfortunately, the parameterization of  $\theta_0$  relies heavily on the  $(d, p)$  data at around 15 MeV, and the uncertainties in these data are quite large, in part because of the low breakup cross section.

### 1. The $(d, p)$ data at around 15 and 25 MeV

The  $^{181}\text{Ta}$  data at 15 MeV [15] were difficult to extract from the published figures because spectra for eight laboratory angles are shown as solid lines that cross each other in ambiguous ways both above and below the absorptive-breakup peaks, making it difficult to estimate the underlying continuum. Another problem is deuteron breakup on the brass detector collimator. A correction for this was made in Ref. [15] by assuming that the 16 deg spectrum was all due to collimator breakup and by subtracting that spectrum, scaled according to the elastic scattering intensity, from the spectra measured at 23 deg and 30 deg. No correction was made at larger angles. Strangely, the spectra at 128 and 170 deg show a peak at an energy slightly below that of the tantalum breakup peak and with about the same width. The intensity is too high for the peaks to be due to breakup on tantalum if the breakup intensity continues to fall off exponentially with detection angle. Similar peaks are visible at 120 and 160 deg in the 25.5 MeV data [7] from the same research group but not for lighter targets in either experiment.

The results for deuteron breakup at 14.8 MeV [6] and 56 MeV [8] do not extend to backward angles, and there is no sign of this peak in the data [17] for 70 and 80 MeV deuterons. DWBA calculations [15] that include both breakup and direct stripping show a backward-angle tail in the double-differential cross section near the energy of the breakup peak, but the energy spectrum of this tail (shown only for a thorium target) is more typical of direct stripping. Instead of a peak at the breakup energy, the cross section increases with the emission energy and

then reaches a plateau. Perhaps the back-angle peaks are due to additional collimator-related background not accounted for in the original data analysis. In the interests of characterizing the forward-angle dip in the cross section relative to the usual exponential fall-off, the back-angle peaks have been treated as background.

The height of the absorptive-breakup peak for the tantalum data at 15 MeV at any given angle was estimated by subtracting a smooth background and, for angles above 30 deg, a correction for the peak observed at 128 and 170 degrees. A range of intensities for the background peak was established by (a) considering it at its strength in the 128-degree spectrum and (b) scaling it linearly with angle using the observed trend between 170 and 128 deg. An average of these two peak intensities was taken. Two considerations favor subtracting this peak. First, without it, the data imply that the forward-angle dip does not reduce the breakup cross section but redistributes it proportionately across the observed angular distribution. Such behavior is incompatible with the  $^3\text{He}$  breakup data. Second, if a similar correction is not made in the 25.5 MeV data, the experimental breakup intensity at 80 deg lies well above the trend from the lighter targets.

The published graph of the platinum data at 14.8 MeV [6] is easier to read, but the data cut off above an emission energy of 12.5 MeV, which is lower than for the other targets. Because the energy of the breakup peak is also higher, there is no clean region for estimating the continuum at the high energy end of the spectrum. At energies below the breakup peak, the curves are similar and often overlapping. In addition, there are no data beyond 85 deg, so it is impossible to look for the kind of back-angle peak seen for tantalum. The detection methods were quite different in the two experiments, so it would be helpful to see if such a peak were observed.

Even with these difficulties, a common trend emerges for tantalum and platinum at around 15 MeV. There appears to be an additional peak at energies 1 to 2 MeV below the energy for absorptive breakup. It is most evident in the platinum data at 12 deg and the tantalum data at 23 and 30 deg, where the absorptive peak is small. Some evidence of a similar peak is also seen in the cadmium data from Ref. [6] at forward angles. This suggests a possible contribution from a breakup mechanism where both fragments are emitted at very nearly the projectile velocity. It is weak enough relative to absorptive breakup only to be seen when the latter is reduced in intensity by the forward-angle dip. An effort was made to subtract this peak when estimating the absorptive breakup contribution in the tantalum data, and the estimated peak intensities at the most forward angles have been assigned large uncertainties. The platinum data have not been used in the quantitative analysis of  $\theta_0$ .

The resulting experimental angular distributions for incident energies around 15 MeV are shown in Fig. 8. In order to determine values for  $\theta_0$  and  $w_{\theta}$ , the angular distributions for zirconium, cadmium, and tantalum were

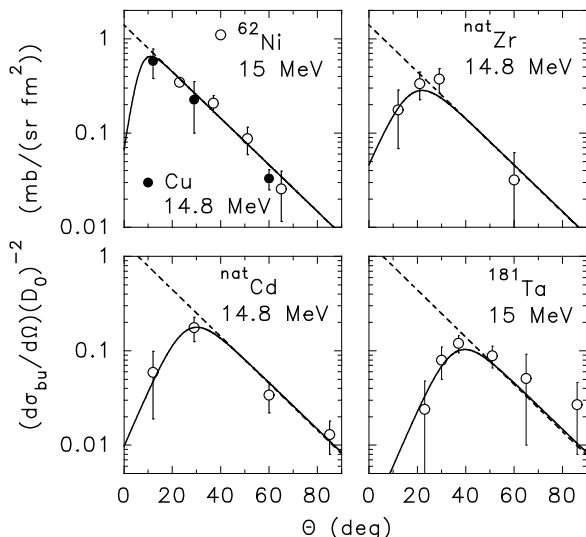


FIG. 8: Angular distributions for the  $(d,p)$  breakup peaks at incident energies of 14.8 and 15.0 MeV. The points show the results obtained from the experimental spectra, the dashed curves show the results for a simple exponential in  $\theta_0$  with the same normalization for all targets, and the solid curves are obtained when the angular barrier is included.

fit using the formula

$$\frac{1}{(D_0)^2} \frac{d\sigma_{bu}}{d\Omega} = K e^{-a_{bu}\theta} T_\theta(\theta), \quad (18)$$

where  $T_\theta$  is given by Eq. (17). The normalization factor  $K$  should be the same for all the targets and was set at  $K = 1.4 \text{ mbsr}^{-1} \text{ fm}^{-2}$ , based on the nickel and copper data. The value of  $w_\theta$  was fixed at 0.09 rad for tantalum and cadmium. This value would be too large for the light targets, where  $\theta_0$  is small, so the width parameter was taken to be

$$w_\theta = \min(0.09 \text{ rad}, \theta_0/3), \quad (19)$$

based on the lack of an observed dip in the nickel-copper data. With these assumptions, values of  $\theta_0$  for the three heaviest targets could be determined.

## 2. The $({}^3\text{He},d)$ data at 70 to 130 MeV

The dip at forward angles is only directly observed in the  $(d,p)$  double-differential cross-section data at around 15 MeV. However, where angular distributions are available, the lack of an observed dip sets an upper limit on  $\theta_0$ . This is the case for  ${}^{90}\text{Zr}({}^3\text{He},d)$  at 70, 90 and 110 MeV [1] and four targets at 130 MeV [2]. Only for  ${}^{197}\text{Au}({}^3\text{He},d)$  at the most forward angle is there an indication of a reduced cross section.

In addition, where data are available for a series of targets at a single forward angle, deviations for heavy

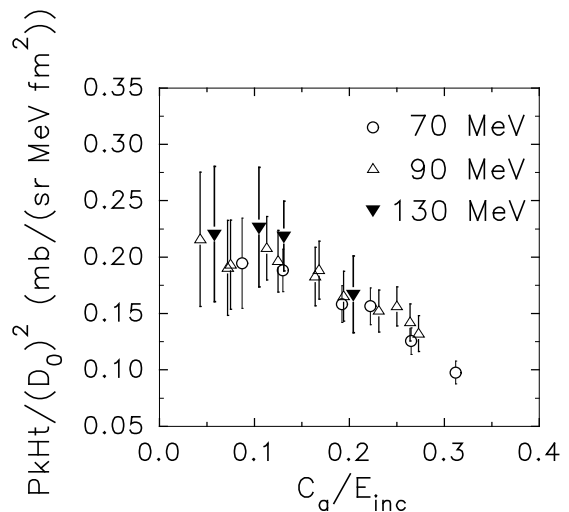


FIG. 9: Normalized peak heights for  $({}^3\text{He},d)$  breakup at 13 deg for 70 and 90 MeV  ${}^3\text{He}$  and 9 deg for 130 MeV  ${}^3\text{He}$ . The 130 MeV points have been divided by a factor of two.

targets from a  $(D_0)^2$  dependence provide evidence of a dip. Plots of estimated peak height divided by  $(D_0)^2$  as a function of  $C_a/E_{inc}$  were made for the 70 and 90 MeV  $({}^3\text{He},d)$  data [1] on a range of targets at 13 deg and, for comparison, for four targets at 130 MeV and 9.0, 10.5, and 12.0 deg [2]. Figure 9 shows fairly constant values for low  $C_a/E_{inc}$ , giving an upper limit to  $\theta_0$ . At higher  $C_a/E_{inc}$ , the normalized peak height decreases, due to the growing influence of the forward-angle dip. Estimates of  $\theta_0$  were obtained by calculating angular distributions for different values of  $\theta_0$  with  $w_\theta$  given by Eq. (19) and by then seeking deviations from a no-dip calculation that matched the observed deviations.

## 3. Parameterization of the dip

The resulting  $\theta_0$  values are summarized in Fig. 10 along with upper limits on  $\theta_0$  obtained from angular distributions where no dip is observed. A single description of  $\theta_0$  for all projectile types was sought, assuming that  $w_\theta$  is given by Eq. (19). The deuteron and  ${}^3\text{He}$  results indicate that  $\theta_0$  is very small at low  $C_a/E_{inc}$ , increases most rapidly around  $C_a/E_{inc} = 0.25$ , and likely approaches an asymptotic value at high  $C_a/E_{inc}$ . The asymptote is higher for deuteron absorptive breakup than for  ${}^3\text{He}$  breakup, and the rise is more rapid. The upper limits for  $\alpha$ -particle breakup are compatible with the more rapid rise in  $\theta_0$  observed for  $d$  absorptive breakup but not with the more gradual rise seen for  ${}^3\text{He}$  unless the asymptote is extremely low. The critical angle is taken to have the form

$$\theta_0 = K_1 \left[ 1 + \exp\left(\frac{K_2 - C_a/E_{inc}}{K_3}\right) \right]^{-1}, \quad (20)$$

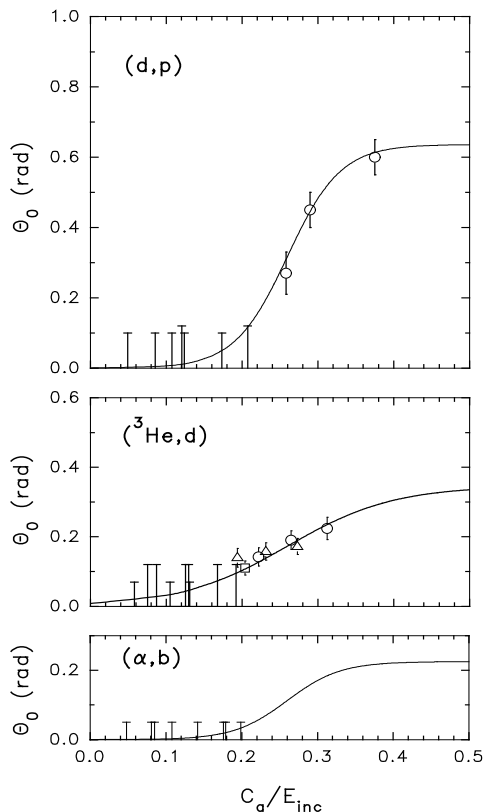


FIG. 10: The critical angle  $\theta_0$  for the forward-angle dip in absorptive breakup. The points show values inferred from the data; the error bars extending up from the X-axis are upper limits. The lines are given by Eq. (21). The  $(d,p)$  results are for incident energies of 15 MeV (circles and one upper limit) and 56 MeV. The  ${}^3\text{He}$  breakup results include data from 70 MeV (circles and three limits), 90 MeV (triangles and three limits), and 130 MeV (square and three limits). For  $\alpha$ -particle breakup, the incident energies are 80, 140, and 160 MeV and the ejectile  $b$  can be any charged particle fragment.

where the  $K$ -values are parameters to be varied.

The empirical values of  $\theta_0$  for  $(d,p)$  and  $({}^3\text{He},d)$  breakup were fit separately, using some constraining points at low  $C_a/E_{\text{inc}}$  to include the influence of the upper limits. The  $K_2$  values were similar and were set at  $K_2 = 0.26$ . The values of  $K_3$  were about a factor of two apart, and the smaller  $K_3$  value was adopted for  $\alpha$  particles, suggesting that  $C_3 = 0.035 Z_a/N_a$ , though this would need to be verified for triton breakup. The asymptotes  $K_1$  for  $d$  and  ${}^3\text{He}$  breakup have a less obvious relationship, but their relative sizes suggest an  $A_a^{-1.5}$  dependence, which was also assumed for incident  $\alpha$  particles. The final formula  $\theta_0$  is

$$\theta_0 = 1.8 \text{ rad } A_a^{-1.5} \left[ 1 + \exp \left( \frac{0.26 - C_a/E_{\text{inc}}}{0.035 Z_a/N_a} \right) \right]^{-1}, \quad (21)$$

which gives the curves shown in Fig. 10. The angle at which the breakup cross section reaches a maximum is

needed to define the maximum laboratory energy for the emitted breakup fragment. For simplicity it is approximated as

$$\theta_{\text{max}} = \theta_0 + w_\theta. \quad (22)$$

The final task was to determine how much the angular barrier reduces the breakup cross section. The integral of  $P_\theta(\theta)$  was evaluated by first considering the sharp-cutoff limit of  $w_\theta = 0$ , in which case the integral is

$$I_0 = e^{-a_{\text{bu}}\theta_0} (\cos \theta_0 + a_{\text{bu}} \sin \theta_0). \quad (23)$$

Then an angle  $\theta_{\text{eff}}$  was sought such that in the  $w_\theta = 0$  limit it gives the same integral as the real distribution with the finite  $w_\theta$ . Experimentation using numerical integration produced the result

$$\theta_{\text{eff}} = \theta_0 + 2.35 a_{\text{bu}} (w_\theta)^2 (I_0 - 0.62). \quad (24)$$

Thus the integral of the real angular distribution probability becomes

$$I_{\text{eff}} = e^{-a_{\text{bu}}\theta_{\text{eff}}} (\cos \theta_{\text{eff}} + a_{\text{bu}} \sin \theta_{\text{eff}}). \quad (25)$$

The calculated angular distributions obtained from Eqs. (15), (17)–(19), (21), and (23)–(25) for  $(d,p)$  breakup at 14.8 and 15 MeV are shown in Fig. 8. The overall normalization was chosen to fit the nickel and copper data and was not adjusted for the other targets. If the same equations are used for  $(d,p)$  breakup at 25.5 MeV, the forward-angle dip occurs at angles below where data are available. The same is true for  ${}^{90}\text{Zr}({}^3\text{He},d)$  at 70 and 90 MeV.

For  $P_\theta(\theta)$  to be a normalized distribution, it should be divided by  $I_{\text{eff}}$ . Therefore, Eq. (16) becomes

$$P_\theta(\theta) = \frac{(a_{\text{bu}})^2 + 1}{2\pi I_{\text{eff}}} e^{-a_{\text{bu}}\theta} T_\theta(\theta) \quad (26)$$

Again it must be emphasized that the results presented here for the Coulomb dip in the angular distributions should be regarded as preliminary. First, they rely heavily on the data for  $(d,p)$  breakup at around 15 MeV, which have large uncertainties, and second, the values of  $C_a/E_{\text{inc}}$  for  $\alpha$ -particle breakup cut off below where the sharp rise in  $\theta_0$  occurs. The  $K_1$  dependence is reasonable in that heavier projectiles should be harder to deflect than lighter ones; the constant  $K_2$  suggests that  $C_a/E_{\text{inc}}$  is a reasonable parameter to use in describing  $\theta_0$ ; but the apparent differences in  $K_3$  have no obvious significance. The utility of this description will be determined as the model is used and tested.

Finally, there is the intriguing question of the back-angle peaks observed in the heaviest targets (tantalum and thorium) in  $(d,p)$  breakup at 15 MeV [15] and 25.5 MeV [7]. If they indeed constitute an additional breakup contribution rather than empirical background, could they contain the cross section that would have occurred in the forward-angle dip but got redistributed into

a much flatter angular distribution? Possibly; the magnitudes are similar. However, until these back-angle peaks are observed by other groups with different experimental techniques and observed for other breakup channels, it is premature to pursue this line of investigation.

## VI. ADDITIONAL BREAKUP PEAK IN THE $(\alpha, d)$ SPECTRA

In order to estimate the total cross section for absorptive breakup, one needs to include the extra peak observed in the  $(\alpha, xd)$  spectra. As noted in Sect. III, the peak's energy, width, and angular distribution are consistent with those for  $(\alpha, p)$  absorptive breakup. This suggests, as hypothesized in Ref. [4], that either a proton breakup fragment picks up a spectator neutron on its way out of the target environment or a neutron fragment picks up a proton. In the latter case, the extra proton would give the same Coulomb acceleration in the exit channel as for the  $(\alpha, p)$  peak, leading to the same peak energy. Perhaps both mechanisms are contributing. For convenience it is designated the  $(\alpha, p, d)$  breakup peak. A similar peak was seen at forward angles in  $({}^3\text{He}, xt)$  spectra with about two-thirds of the projectile energy [21, 22] and was thought to possibly represent  $({}^3\text{He}, d)$  breakup followed by the deuteron picking up a spectator neutron.

The intensity of the  $(\alpha, p, d)$  peak is difficult to estimate because of uncertainties in the underlying continuum. Qualitatively, however, the 160 MeV spectra show that as the targets get heavier, the extra peak gets weaker relative to the main  $(\alpha, d)$  breakup peak, so the cross section likely varies more nearly with  $D_0$  than with  $(D_0)^2$ . Interestingly, even though Ref. [4] found an  $A^{1/3}$  (or roughly  $D_0$ ) dependence for the main breakup cross section, it agrees that the extra peak has a weaker dependence on target mass. Additionally, Ref. [21] found that the cross section for the broad peak they observed in  $({}^3\text{He}, t)$  spectra at forward angles scaled roughly with  $A^{1/2}$  with an  $A^{1/3}$  dependence also possible. The latter is nearly consistent with the  $D_0$  dependence suggested here.

If the proposed mechanism is correct, then similar peaks should be evident in  $({}^3\text{He}, xd)$ ,  $(t, xd)$ , and  $(d, xd)$  spectra at very forward angles. The best place in the current database to observe it is in the  ${}^{27}\text{Al}({}^3\text{He}, xd)$  spectra measured at 130 MeV. While there is no obvious peak at the energy of the  $({}^3\text{He}, p)$  breakup peak, without the presence of this contribution, the implied continuum under the main breakup peak would be inconsistent with the general behavior of preequilibrium spectra. A more realistic, relatively flat continuum for emission energies between 20 and 60 MeV suggests the presence of an extra peak at the energy of the  $({}^3\text{He}, p)$  absorptive-breakup peak.

Based on these observations, the extra peak is assumed to occur in all the inclusive deuteron spectra and to be characterized by the peak energy, shape, and angular dis-

tribution of the corresponding proton fragment. However the cross section is assumed to be proportional to  $D_0$  rather than  $D_0^2$ .

## VII. TOTAL BREAKUP CROSS SECTION

This leaves the dependence of the breakup cross section on the incident energy and breakup channel still to be determined. If the absorptive breakup cross section in a given breakup channel is set equal to  $(D_0)^2$  in a model calculation, then the ratio of the experimental peak height to the calculated peak height should give  $\sigma_{\text{ab}}(E_{\text{inc}})/(D_0)^2$ , where  $\sigma_{\text{ab}}$  is the cross section for  $(a, b)$  absorptive breakup. Figure 11 shows the averages of these ratios for the available targets. Here the data from Table I have been supplemented with three additional crude points: one from  ${}^{57}\text{Fe}$  and  ${}^{61}\text{Ni}({}^3\text{He}, p)$  at 25.6 MeV [23]; one from  ${}^{61}\text{Ni}({}^3\text{He}, n)$  at 25.6 MeV [23]; and one from  ${}^{\text{nat}}\text{Al}$  and  ${}^{\text{nat}}\text{Zr}(\alpha, n)$  at 140 MeV [24]. The normaliza-

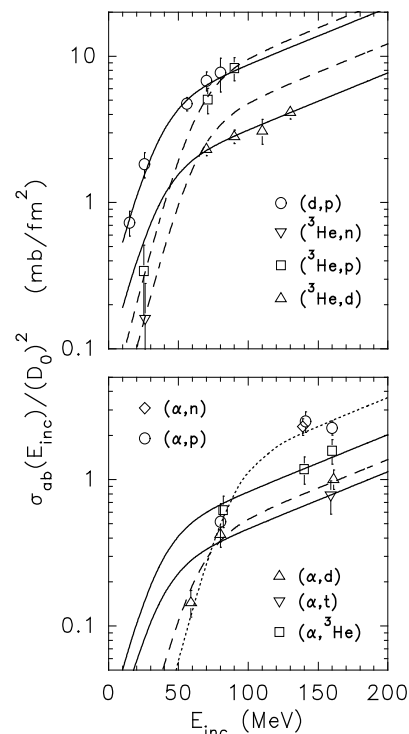


FIG. 11: Average normalization factors  $\sigma_{\text{ab}}(E_{\text{inc}})/(D_0)^2$  for the breakup peaks in the indicated breakup channels as a function of the projectile energy. The solid, dashed, and dotted curves show the model values for  $A_a - A_b = 1, 2, \text{ and } 3$ , respectively.

tion factors in the figure are strongly dependent on the angular distribution systematics, especially for those reactions in which the angular distribution falls off most rapidly with angle. Changing either the slope parameter or  $\theta_0$  can significantly change the normalization required.

These results should be regarded as tentative and part of a model “package.”

Figure 11 shows that the standard absorptive breakup cross section for all channels has an initial barrier at low energies and then approaches an exponential increase. Therefore, the breakup cross section is written as

$$\sigma_{\text{ab}}(E_{\text{inc}}) = \mathcal{N}_{\text{ab}} I_{\text{eff}} (D_0)^2 \exp\left(\frac{E_{\text{inc}}}{K_{\sigma} \text{ MeV}}\right) T_{\sigma}(E_{\text{inc}}) \times \int P_{\text{E}}^{(\text{ab})}(E) dE, \quad (27)$$

where,  $\mathcal{N}_{\text{ab}}$  is the channel-specific normalization,  $K_{\sigma}$  describes the asymptotic exponential, which is assumed to be the same for all breakup channels, and  $T_{\sigma}$  is the barrier-penetrability factor. The factor  $I_{\text{eff}}$  accounts for any reduction in the breakup cross section by the forward-angle dip, and the integral over  $P_{\text{E}}(E)$  accounts for any reduction due to the exit-channel Coulomb barrier. If the barrier in Eq. (27) has a height  $E_{1/2}$  and width  $w_{\sigma}$ , then  $T_{\sigma}$  can be written as

$$T_{\sigma}(E_{\text{inc}}) = \left[1 + \exp\left(\frac{E_{1/2} - E_{\text{inc}}}{w_{\sigma}}\right)\right]^{-1}. \quad (28)$$

The width was assumed to be independent of the breakup channel, while  $E_{1/2}$  increases with  $A_{\text{a}} - A_{\text{b}}$ . Given that there are four parameters ( $\mathcal{N}_{\text{ab}}$ ,  $K_{\sigma}$ ,  $E_{1/2}$ , and  $w_{\sigma}$ ) for each breakup channel and that the maximum number of data points for a given channel is only four, an iterative fitting method was used. The resulting cross section for absorptive breakup is

$$\sigma_{\text{ab}}(E_{\text{inc}}) = \mathcal{N}_{\text{ab}} I_{\text{eff}} (D_0)^2 \exp\left(\frac{E_{\text{inc}}}{112 \text{ MeV}}\right) T_{\sigma}(E_{\text{inc}}) \times \int P_{\text{E}}^{(\text{ab})}(E) dE, \quad (29)$$

$$T_{\sigma}(E_{\text{inc}}) = \left[1 + \exp\left(\frac{E_{1/2} - E_{\text{inc}}}{13 \text{ MeV}}\right)\right]^{-1}, \quad (30)$$

$$E_{1/2} = 34 \text{ MeV} (A_{\text{a}} - A_{\text{b}})^{0.84}. \quad (31)$$

The  $\mathcal{N}_{\text{ab}}$  values are given in Table III, and the resulting curves for  $\sigma_{\text{a,b}}/(D_0)^2$  are shown in Fig. 11.

As has been seen, the deuteron-fragment spectra show an additional breakup peak at the energy of a proton fragment from absorptive breakup. This is attributed to a nucleon fragment picking up a complementary nucleon to form a deuteron as it exits the reaction zone. The cross section for this additional deuteron peak has the same form as Eq. (29) but with a factor of  $D_0$  rather than  $(D_0)^2$  so that

$$\sigma_{\text{apd}}(E_{\text{inc}}) = \mathcal{N}_{\text{apd}} I_{\text{eff}} D_0 \exp\left(\frac{E_{\text{inc}}}{112 \text{ MeV}}\right) T_{\sigma}(E_{\text{inc}}) \times \int P_{\text{E}}^{(\text{ap})}(E), \quad (32)$$

TABLE III: Channel specific normalization constants  $\mathcal{N}_{\text{ab}}$  for the breakup cross section. The  $({}^3\text{He},n)$  value is not well determined and is set to about half the  $({}^3\text{He},p)$  value, in keeping with the numbers of protons and neutrons in the projectile. The indicated “sister channels” are ones for which no data were available and whose normalization constants are set to those of the corresponding main channel.

breakup channel	$\mathcal{N}_{\text{ab}}$ (mb/fm <sup>2</sup> )	sister channel
( <i>d,p</i> )	3.6	( <i>d,n</i> )
( <sup>3</sup> He, <i>n</i> )	(2.0)	( <i>t,p</i> )
( <sup>3</sup> He, <i>p</i> )	4.1	( <i>t,n</i> )
( <sup>3</sup> He, <i>d</i> )	1.3	( <i>t,d</i> )
( $\alpha,n$ ),( $\alpha,p$ )	0.61	
( $\alpha,d$ )	0.23	
( $\alpha,t$ )	0.19	
( $\alpha,{}^3\text{He}$ )	0.34	

where  $T_{\sigma}$  is evaluated using the  $E_{1/2}$  value for the corresponding proton breakup fragment. This peak, observed for  $\alpha$ -particle and <sup>3</sup>He breakup, is also assumed to occur for incident deuterons and tritons. Preliminary normalization factors were set based on the data from <sup>27</sup>Al( $\alpha, d$ ) at 160 MeV and <sup>27</sup>Al(<sup>3</sup>He,*d*) at 130 MeV. Additional adjustments during the data comparisons finally led to values of  $\mathcal{N}_{\text{apd}} = 1.2$  and  $\mathcal{N}_{3\text{Hepd}} = 1.8$ . Values for the corresponding deuteron- and triton-induced breakup are unknown and have been tentatively set at unity.

These expressions for the absorptive breakup cross section should be used with caution at higher incident energies. At some point the cross section is likely to level off because it cannot exceed the total reaction cross section. The importance of projectile breakup as a fraction of the total reaction cross section is examined in Sect. IX, after the validity of the model has been evaluated through comparisons with data.

## VIII. COMPARISONS WITH EXPERIMENT

The present model for absorptive projectile breakup is based on average trends over an extended database and needs to be compared with data for specific reactions. An estimate of the continuum cross section underlying the breakup peak was drawn by matching the experimental spectrum above and below the breakup peak(s) and, when possible, being guided by the measured spectra at larger angles where the breakup cross section is negligible. In general, the calculations reproduce the main features but not the details of the data, as one would expect from the global nature of the model.

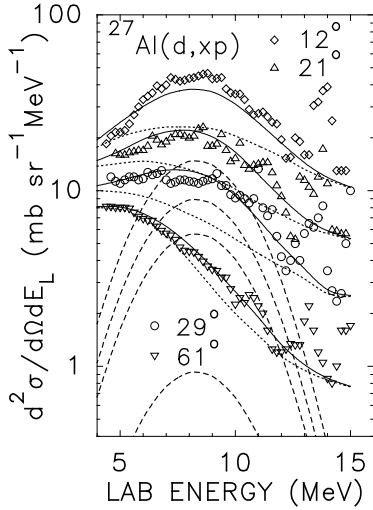


FIG. 12: Comparison of measured double-differential spectra with calculated breakup peaks and an estimated continuum for  $^{27}\text{Al}(d,xp)$  at 14.8 MeV. The points show the data from Ref. [6], the dashed curves show the calculated breakup peaks, the dotted curves show estimates of the underlying continuum, and the solid curves show the total estimated spectra.

#### A. Deuteron breakup at around 15 MeV

For deuteron breakup at around 15 MeV, comparisons between calculation and experiment for some of the lighter targets are shown in Figs. 12 to 14. The agreement is reasonable given the low breakup cross section and the difficulties in estimating the underlying continuum. Figure 15 shows the results for tantalum. The problems associated with extracting these data from the published graph were discussed in Sect. V C 1. The agreement at the two most forward angles (23 and 30 deg) looks quite poor, but much of that is due to the presence of what is assumed to be a dissociative breakup component present in the data. A rough correction for this was made in Fig. 8, but this peak is not included in the current fits. The data at 37 and 51 deg are well accounted for, but the data at larger angles are underestimated.

#### B. Deuteron breakup at 56 MeV

The data at 56 MeV for  $(d,p)$  breakup [8] are particularly useful because they comprise a large number of targets, include angles down to 9.5 deg, and have an incident energy in a range of interest for the FENDL-3 database. Comparisons are shown in Figs. 16 to 18. The level of agreement here is better than around 15 MeV because of the higher breakup cross section and the absence of the dip at forward angles. For  $^{118}\text{Sn}$  (Fig. 17) the experimental breakup peak shifts to lower energies as the emission angle increases, while the data on  $^{27}\text{Al}$  (Fig. 16),  $^{58}\text{Ni}$ , and  $^{90}\text{Zr}$  have the peak remaining at a constant energy.

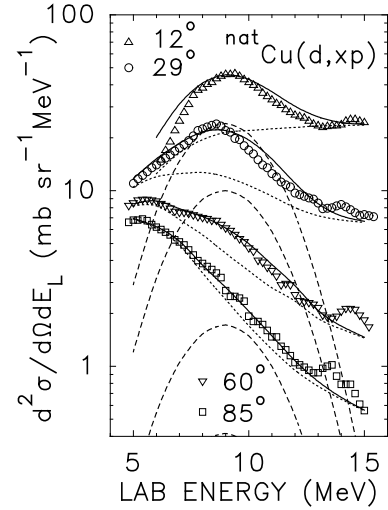


FIG. 13: Comparison between experimental results and the current breakup model for  $^{\text{nat}}\text{Cu}(d,xp)$  at 14.8 MeV. The points and curves have the same significance as in Fig. 12.

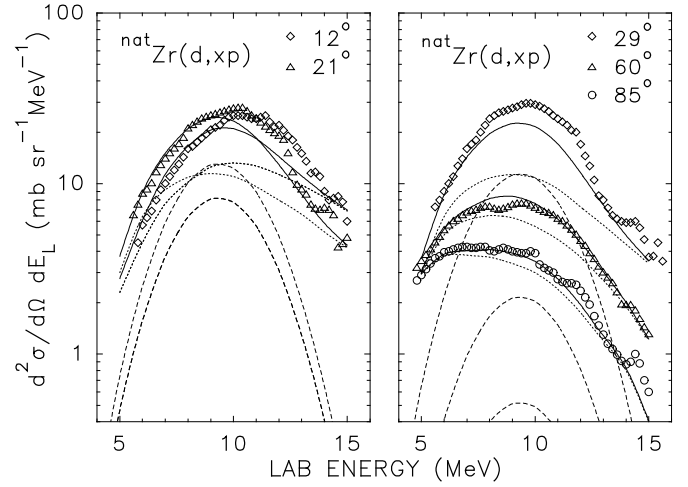


FIG. 14: Comparison between experimental results and the current breakup model for  $^{\text{nat}}\text{Zr}(d,xp)$  at 14.8 MeV. The points and curves have the same significance as in Fig. 12.

The bismuth data (Fig. 18) show either a second peak at lower energies or a shoulder on the main absorptive-breakup peak. The published spectra at 9.5 deg for the gold, tantalum, and even terbium targets show a similar structure. The implied energy separation is too large for the structure to be due to dissociative breakup, and its origin is not understood. Overall, however, variation of the breakup peak with emission energy, angle, and target mass in this data set is reasonably well accounted for by the model, as is the magnitude of the breakup cross section.

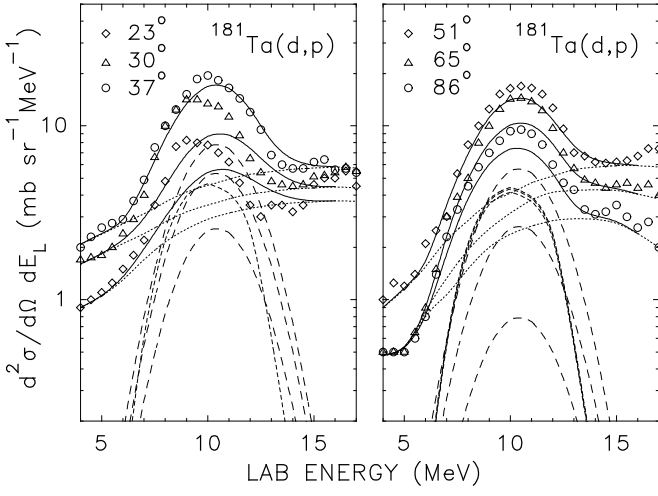


FIG. 15: Comparison between experimental results and the current breakup model for  $^{181}\text{Ta}(d,p)$  at 15.0 MeV. The points and curves have the same significance as in Fig. 12 except that the data are from Ref. [15] and the short-dash curves for angles greater than  $30^\circ$  show an extrapolation of the breakup-like peak observed at backward angles. The data are in the center-of-mass system, but for such a heavy target the differences between the laboratory and center-of-mass systems are small.

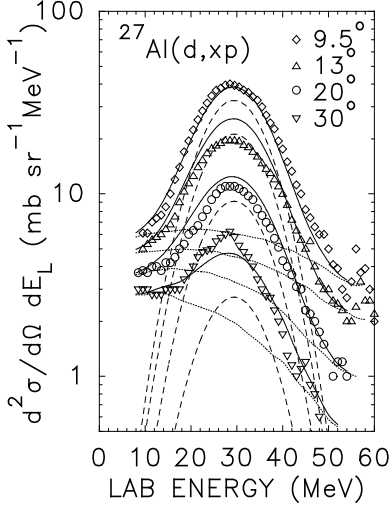


FIG. 16: Comparison between experimental double-differential cross sections from Ref. [8] and the current breakup model for  $^{27}\text{Al}(d,xp)$  at 56.0 MeV. The points and curves have the same significance as in Fig. 12.

### C. ( $^3\text{He},d$ ) breakup at 70 to 130 MeV

The data on ( $^3\text{He},d$ ) breakup includes results at 70, 90, and 110 MeV [1] and at 130 MeV [2]. The published data of Matsuoka *et al.* [1] consist of energy spectra measured at several forward angles for a  $^{90}\text{Zr}$  target, plus spectra at a laboratory angle of 13 deg for a variety of targets at

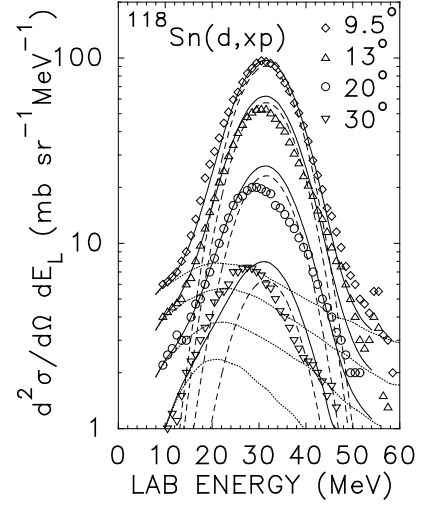


FIG. 17: Comparison between experimental double-differential cross sections from Ref. [8] and the current breakup model for  $^{118}\text{Sn}(d,xp)$  at 56.0 MeV. The points and curves have the same significance as in Fig. 12.

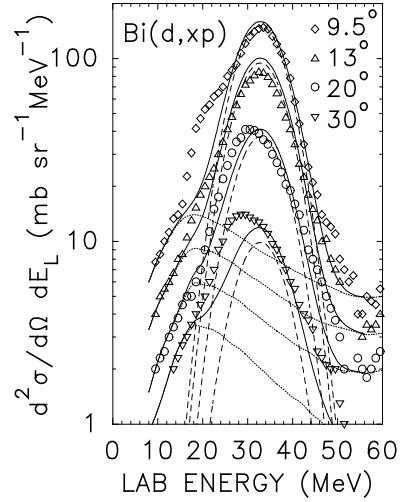


FIG. 18: Comparison between experimental double-differential cross sections from Ref. [8] and the current breakup model for  $^{209}\text{Bi}(d,xp)$  at 56.0 MeV. The points and curves have the same significance as in Fig. 12.

70 and 90 MeV. The 130 MeV data of Djaloeis *et al.* [2] cover a range of angles for four targets. The published graphs for both data sets show spectra from all angles for a given target or from all targets at a fixed angle using a single linear scale. Therefore the data for the larger angles or lighter targets (the ones with smaller breakup cross sections) are compressed and more difficult to extract.

Fits to the zirconium data at 70 and 110 MeV are shown in Figs. 19 and 20. Results at 90 MeV are similar except that the data at 20 and 30 deg are more seri-

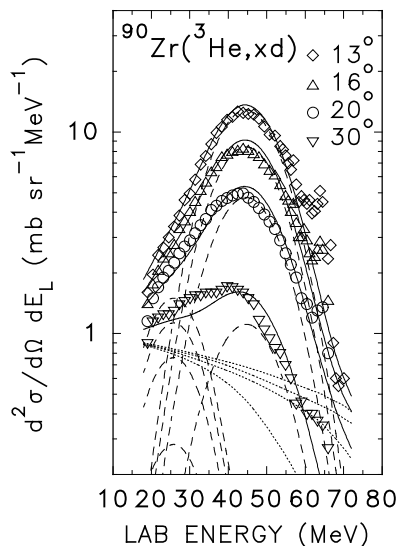


FIG. 19: Comparison between experimental double-differential cross sections from Ref. [1] and the current breakup model for  $^{90}\text{Zr}(^3\text{He},d)$  at 70 MeV. The points and curves have the same significance as in Fig. 12.

ously underestimated at emission energies below about 60 MeV. The agreement between model and experiment is generally good, and the contribution of the additional ( $^3\text{He},p,d$ ) breakup peak increases with increasing bombarding energy. However, there is extra experimental cross section between the two breakup peaks. It is most evident at the larger angles, where the breakup cross section is low. This question is discussed further in connection with the 130 MeV data.

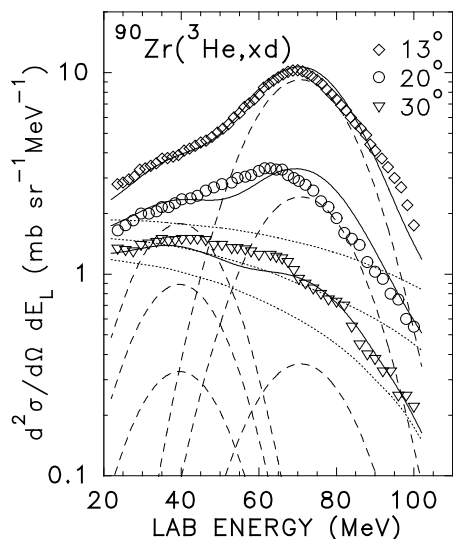


FIG. 20: Comparison between experimental double-differential cross sections from Ref. [1] and the current breakup model for  $^{90}\text{Zr}(^3\text{He},d)$  at 110 MeV. The points and curves have the same significance as in Fig. 12.

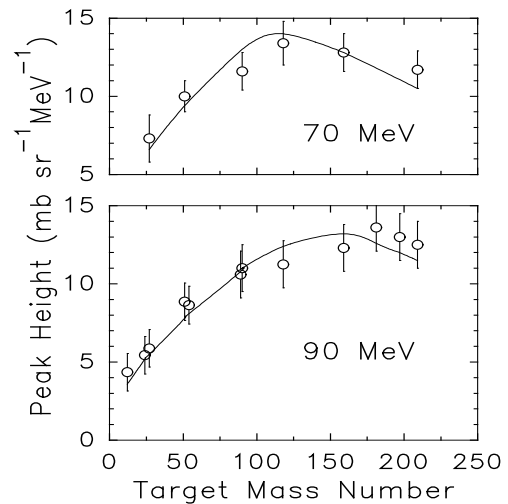


FIG. 21: Comparison of experimental and calculated peak heights for ( $^3\text{He},d$ ) absorptive breakup at  $13^\circ$  and the indicated incident energies. The points show the experimental values; the curves connect the model points for the same targets.

The target mass dependence at 70 and 90 MeV is shown in Fig. 21, where the height of the main breakup peak at  $13^\circ$  is shown as a function of target mass number. For the lighter targets, the peak height increases as  $(D_0)^2$ . The leveling off and then decrease for the heavier targets is due to the forward-angle dip in the breakup cross section. This dip is less important at higher incident energies—a trend that is reasonably well reproduced by the model.

Comparisons with the double-differential cross section data for cobalt and gold at 130 MeV [2] are shown in Figs. 22 and 23. Results for aluminum and niobium are similar except that the spectrum for  $^{27}\text{Al}$  at  $21^\circ$  looks as if it had been taken at a smaller angle. Agreement at  $7.5$  to  $12^\circ$  is generally good for all targets, while agreement at  $15^\circ$  and especially  $21^\circ$  improves with increasing target mass. Part of this is because all the targets at  $15^\circ$  and  $21^\circ$  give evidence of extra cross section that (except for  $^{27}\text{Al}$  at  $21^\circ$ ) appears to peak at about half the projectile energy. This, therefore, looks like a more extreme case of what was observed at 70 to 110 MeV. Since the breakup cross section increases with target mass number, this additional cross section is most evident for the lighter targets. The gold data at  $9^\circ$  shows the effect of the angular barrier, and this is reproduced by the model. The role played by the extra ( $^3\text{He},p,d$ ) breakup peak is clear, even though this peak was introduced based on observations in the  $(\alpha,d)$  data.

To investigate the extra cross section, the fit curves at all four incident energies were subtracted from the data in the region between the two breakup peaks. Only the most forward angles were excluded, because the large breakup peaks obscure the extra cross section. There

is much uncertainty in the results. This cross section sits on the wings of both breakup peaks and therefore the estimates of it depend on how well each calculated breakup peak describes the data. However, trends can be observed in the midst of the uncertainty. The cross section peaks at roughly half the projectile energy. Its intensity is largely constant with emission angle and is independent of the target mass at 130 MeV. There is no clear trend of intensity between 70 and 110 MeV, but the average intensity at an emission energy of  $E_{\text{inc}}/2$  is  $0.5 \pm 0.25$  mb/(sr MeV), while the average value at 130 MeV is  $1.25 \pm 0.15$ . Here the errors are just those due to averaging, not to variations in how well the model curves reproduce the data near the breakup peaks. The origin of this extra cross section is unclear, but its presence is what produced the observed deviations from the usual angular distribution systematics for  $^{27}\text{Al}$  and  $^{59}\text{Co}$  that were noted in Sect. V.

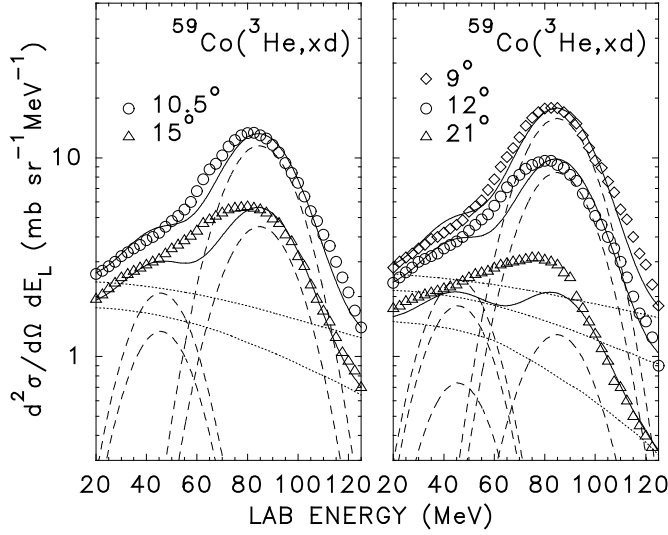


FIG. 22: Comparison between experimental double-differential cross sections from Ref. [2] and the current breakup model for  $^{59}\text{Co}(^3\text{He},d)$  at 130 MeV. The points and curves have the same significance as in Fig. 12.

#### D. ( $^3\text{He},p$ ) breakup at 70 and 90 MeV.

The available data on ( $^3\text{He},p$ ) [1], consist of spectra measured at several forward angles for 70 and 90 MeV  $^3\text{He}$  incident on  $^{90}\text{Zr}$ . The comparisons with the model breakup peaks show good agreement at both energies. The 90 MeV results are shown in Fig. 24.

#### E. ( $\alpha,d$ ) breakup at 80 and 160 MeV

The breakup of incident  $\alpha$  particles is more difficult to verify. The scatter and structure in the data make

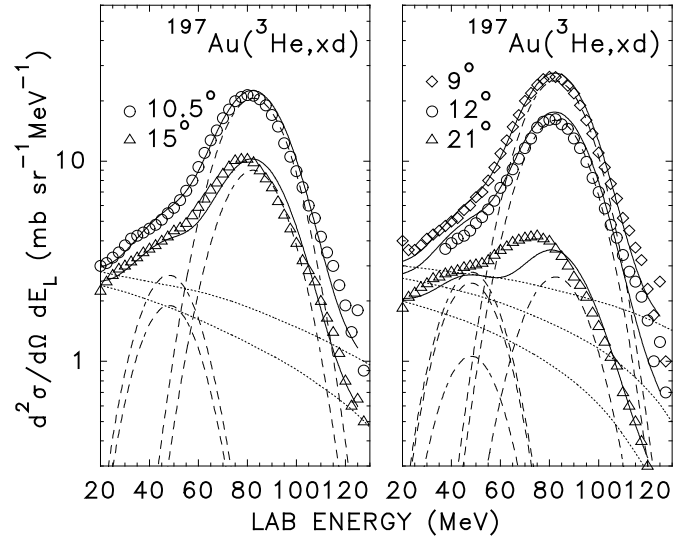


FIG. 23: Comparison between experimental double-differential cross sections from Ref. [2] and the current breakup model for  $^{197}\text{Au}(^3\text{He},d)$  at 130 MeV. The points and curves have the same significance as in Fig. 12.

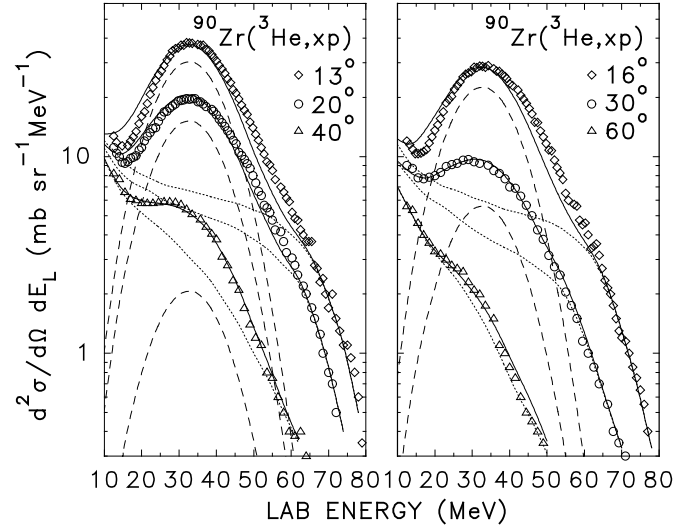


FIG. 24: Comparison between experimental double-differential cross sections from Ref. [1] and the current breakup model for  $^{90}\text{Zr}(^3\text{He},d)$  at 90 MeV. The points and curves have the same significance as in Fig. 12.

it hard to draw a continuum under the peaks. In addition, the peaks for the proton and mass-three fragments occur close to the low and high emission-energy ends of the spectrum, respectively, making one end of the continuum especially uncertain. The ( $\alpha,xd$ ) data are therefore the easiest to study and are discussed first. For all breakup channels, guidance in drawing the underlying continuum is provided by the spectra at angles with minimal breakup contributions.

In the study of the peak energies, Fig. 3 showed that the experimental positions of the main breakup peak in the  $(\alpha,xd)$  data tend to be a few MeV above the calculated energy from the model for the 80 MeV data, where the errors on the experimental estimates are small. This difference is clearly seen in Fig. 25. Thus for all of the measured spectra, calculations have been performed using both the nominal peak energy for the main breakup peak and an energy 4 MeV higher. Figure 26 shows that the shift of 4 MeV gives a much better description of the data, but there is no obvious physical reason for it, given that Coulomb energy shifts in the entrance and exit channels should cancel out. Figures 25 and 26 also show the role of the  $(\alpha,p,d)$  breakup peak.

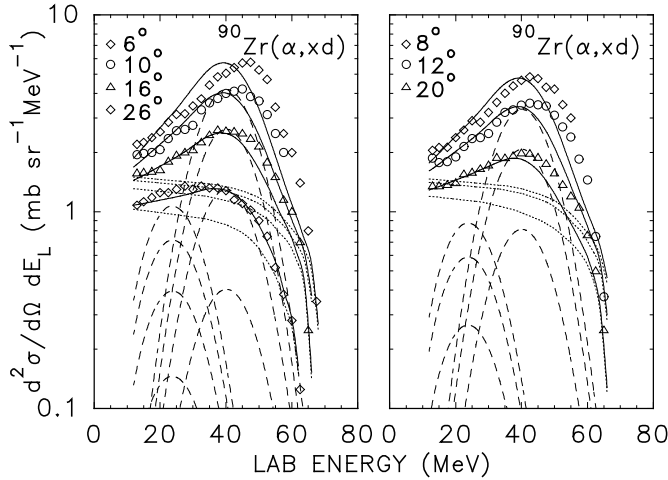


FIG. 25: Comparison between experimental double-differential cross sections from Ref. [4] and the current breakup model for  $^{90}\text{Zr}(\alpha,xd)$  at 80 MeV. The points and curves have the same significance as in Fig. 12 except that the lower energy calculated breakup peak in each spectrum is the  $(\alpha,p,d)$  breakup peak.

The  $(\alpha,p,d)$  peak becomes more evident at  $E_{\text{inc}} = 160$  MeV, where again the calculated main breakup peaks have been shifted up in energy by 4 MeV. Figure 27 shows the results for  $^{58}\text{Ni}$  and are similar to the agreement found for the  $^{27}\text{Al}$  and  $^{90}\text{Zr}$  targets. The two breakup peaks in each spectrum are clearly visible, and drawing in a reasonable (though not definitive) continuum yields good agreement with the data. In the corresponding results for  $^{209}\text{Bi}$  in Fig. 28, the calculated angular distribution of the  $(\alpha,p,d)$  peak is slightly too steep.

In balance, the measured  $(\alpha,xd)$  data at very forward angles are fairly well reproduced using the present model for absorptive breakup and a reasonable estimate of the underlying continuum, especially if the main breakup peak is shifted up in energy by about 4 MeV.

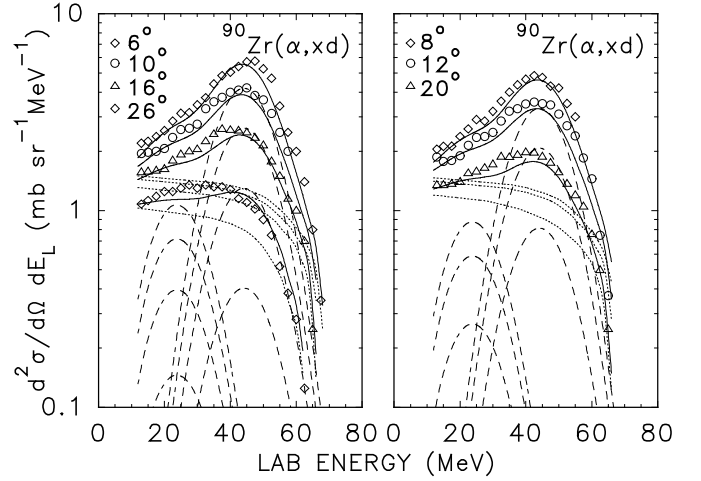


FIG. 26: The same comparison as in Fig. 25, except that the upper or main calculated breakup peak is shown shifted up by 4 MeV from the energy given by the systematics of the present model.

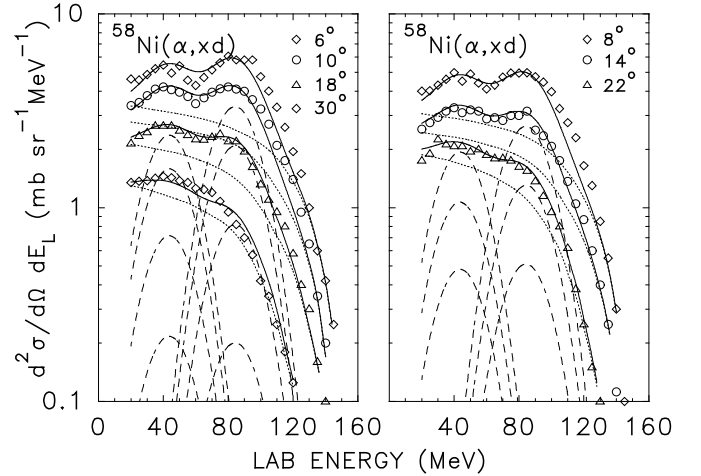


FIG. 27: Comparison between experimental double-differential cross sections from Ref. [4] and the current breakup model for  $^{58}\text{Ni}(\alpha,xd)$  at 160 MeV. The points and curves have the same significance as in Fig. 12 but with the inclusion of the calculated  $(\alpha,p,d)$  breakup peak. The upper or main peak is shown shifted up by 4 MeV from the peak energy given by the present model.

#### F. $(\alpha,p)$ breakup at 80 and 160 MeV

The main difficulty in the  $(\alpha,p)$  breakup channel is that the breakup peak lies just above the low-emission-energy cutoff in the data. In addition, at an incident energy of 160 MeV, the data for both the zirconium and bismuth targets display a much narrower peak on the low-energy side of the breakup peak at the three most forward angles. As a result, the continua drawn under the breakup peaks were guided by the shape of the measured

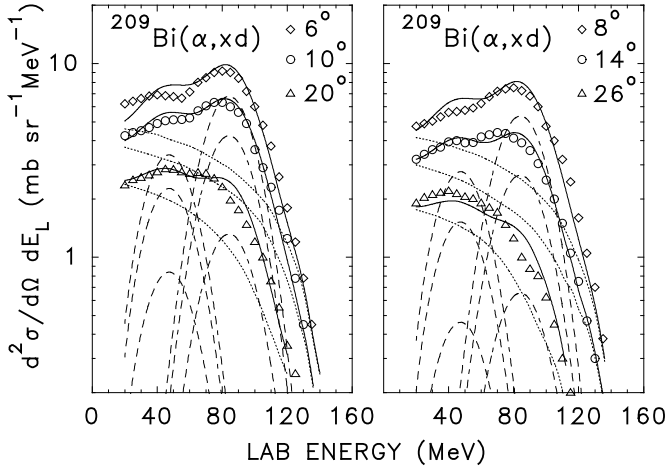


FIG. 28: Comparison between experimental double-differential cross sections from Ref. [4] and the current breakup model for  $^{209}\text{Bi}(\alpha,xd)$  at 160 MeV. The points and curves have the same significance as in Fig. 12 but with the inclusion of the calculated  $(\alpha,p,d)$  breakup peak. The upper or main peak is shown shifted up by 4 MeV from the peak energy given by the present model.

spectrum at the largest observation angle.

Results for  $^{90}\text{Zr}$  at 80 MeV and for  $^{27}\text{Al}$  and  $^{58}\text{Ni}$  at 160 MeV are shown in Figs. 29 to 31. The agreement is generally good.

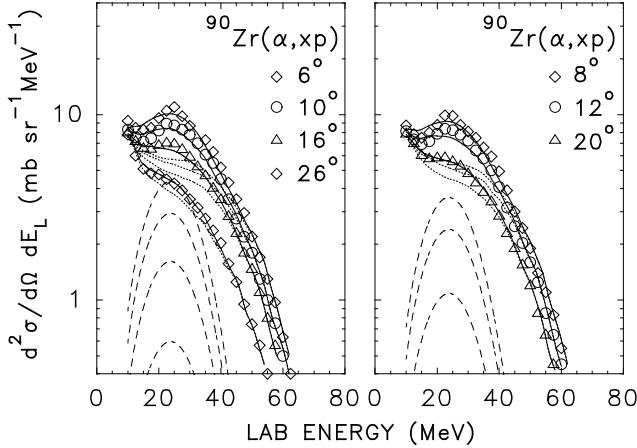


FIG. 29: Comparison between experimental double-differential cross sections from Ref. [4] and the current breakup model for  $^{90}\text{Zr}(\alpha,xp)$  at 80 MeV. The points and curves have the same significance as in Fig. 12.

### G. $(\alpha,t)$ and $(\alpha,^3\text{He})$ breakup at 80, 140, and 160 MeV

For the mass-three breakup fragments, the data from Ref. [4] at an incident energy 80 MeV have a large number

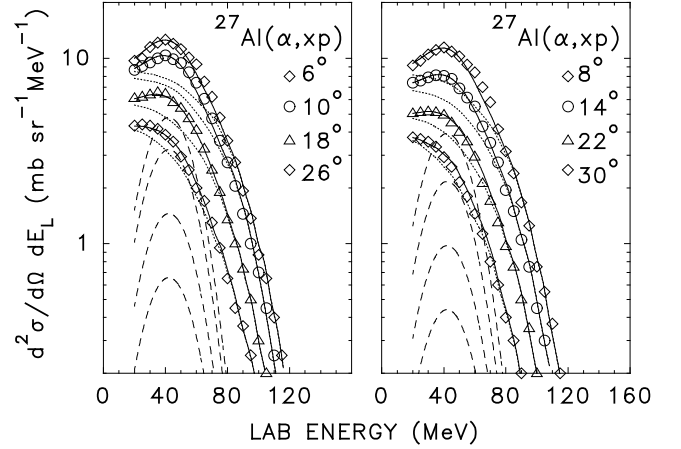


FIG. 30: Comparison between experimental double-differential cross sections from Ref. [4] and the current breakup model for  $^{27}\text{Al}(\alpha,xp)$  at 160 MeV. The points and curves have the same significance as in Fig. 12.

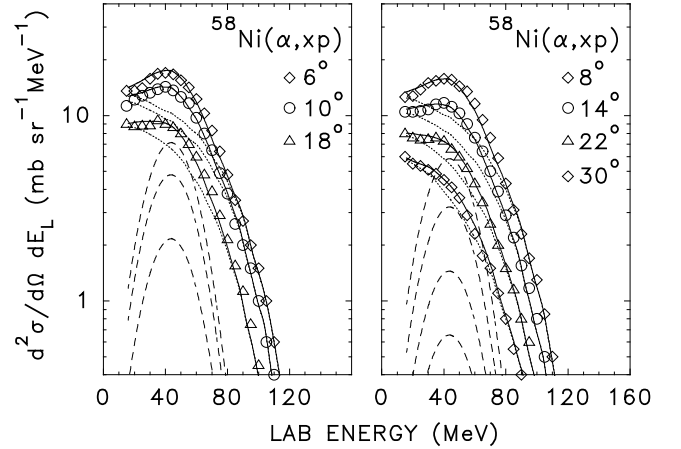


FIG. 31: Comparison between experimental double-differential cross sections from Ref. [4] and the current breakup model for  $^{58}\text{Ni}(\alpha,xp)$  at 160 MeV. The points and curves have the same significance as in Fig. 12.

of sharp peaks in the area of the breakup cross section, making comparisons with the model problematic. At 160 MeV, the data for  $^{27}\text{Al}$  are the cleanest, and results are shown in Figs. 32 and 33. The shape of the continuum underlying the breakup peaks is determined mostly by the 26 deg data, where the breakup peak is negligible but the data are the hardest to read on the published graphs. Over all, the agreement is good.

Figure 34 shows comparisons for the 140 MeV  $(\alpha,^3\text{He})$  reaction on bismuth, using data from Ref. [3]. The continuum is harder to estimate here because the largest data angle still has significant breakup cross section and because the data are cut off below about 45 MeV. A continuum shape similar to the one seen in Fig. 33 has been assumed. Because of the large Coulomb barrier for

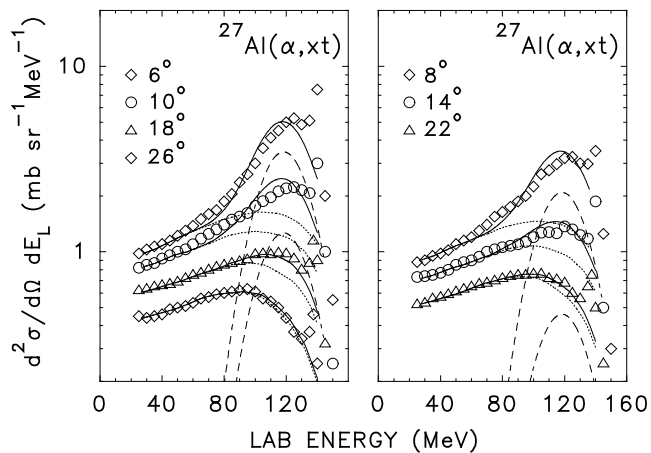


FIG. 32: Comparison between experimental double-differential cross sections from Ref. [4] and the current breakup model for  $^{27}\text{Al}(\alpha,xt)$  at 160 MeV. The points and curves have the same significance as in Fig. 12.

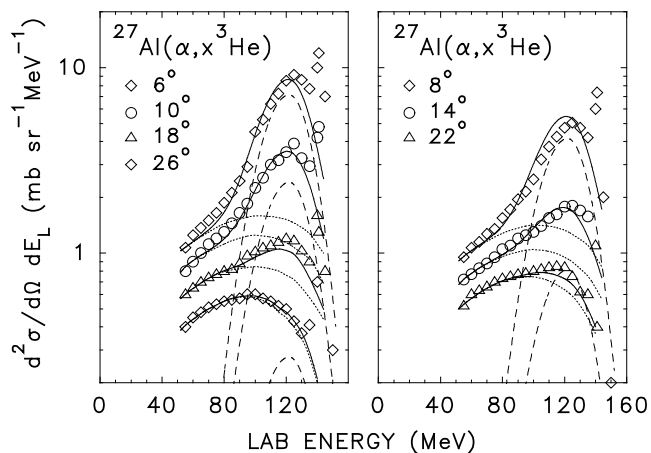


FIG. 33: Comparison between experimental double-differential cross sections from Ref. [4] and the current breakup model for  $^{27}\text{Al}(\alpha,x^3\text{He})$  at 160 MeV. The points and curves have the same significance as in Fig. 12.

bismuth, the Coulomb shift in the peak energy causes the breakup peak to be noticeably asymmetric, and the model accounts for this distortion. A much smaller and less obvious asymmetry is seen in the corresponding aluminum results in Fig. 33.

## IX. IMPORTANCE OF PROJECTILE BREAKUP

### A. Current results

Having derived a global model for absorptive projectile breakup—the dominant breakup mechanism—for projectiles with mass numbers 2, 3, and 4, and having verified

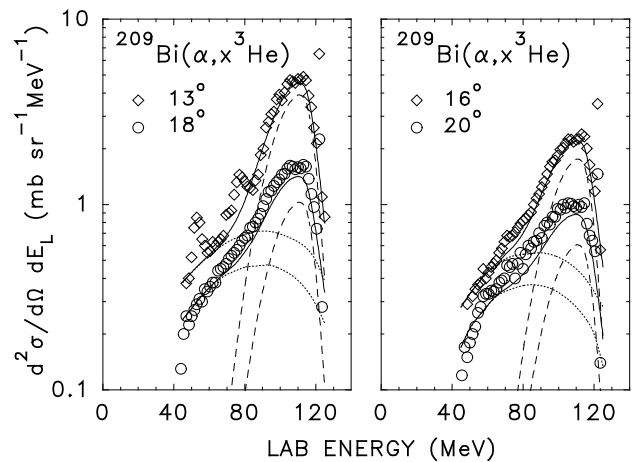


FIG. 34: Comparison between experimental double-differential cross sections from Ref. [3] and the current breakup model for  $^{209}\text{Bi}(\alpha,x^3\text{He})$  at 140 MeV. The points and curves have the same significance as in Fig. 12.

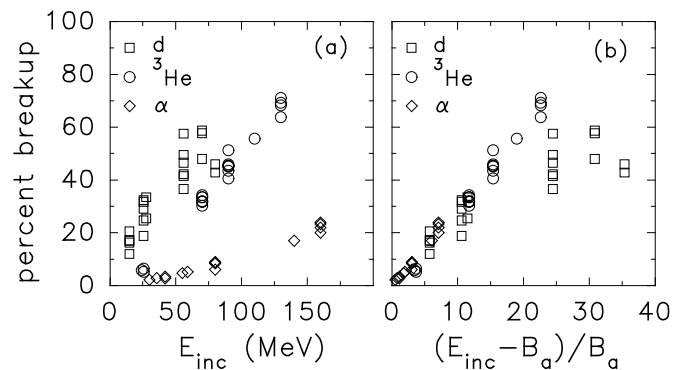


FIG. 35: Percentage of the total reaction cross section due to absorptive breakup as calculated in the current model shown, (a) as a function of the projectile energy in the laboratory system and (b) as a function of the ratio  $(E_{\text{inc}} - B_a)/B_a$ . The points show the results for individual target-projectile combinations in the database.

that it reproduces the general trends observed in data from the literature, it is time to compare the total cross section for absorptive breakup summed over all possible emission fragments with the total reaction cross section. This is done in Fig. 35(a), where the estimates of the total reaction cross section are taken from the values used in the preequilibrium reaction computer code PRECO [25]. These results include the additional  $(a, p, d)$  breakup peak seen in the deuteron emission spectra.

Four observations can be made. First, even though there is considerable spread in the results for a given projectile and incident energy, particularly for deuteron breakup, the results for each projectile show a well-defined and distinct trend. Second, the percent breakup at a given incident energy decreases as the internal bind-

ing energy of the projectile increases. Third the trend for each projectile tends toward zero at an incident energy close to the energy required to break the projectile into two fragments, and it increases as the incident energy increases. At the higher energies, the deuteron results seem to start flattening, as these curves must because the breakup cross section cannot exceed the total reaction cross section. Fourth, at a given incident energy, the percent deuteron breakup in the total reaction cross section generally increases significantly with target mass, a trend not observed for the other projectiles.

Because it looks as if the energy scale in Fig. 35(a) spreads out roughly with the projectile's internal binding energy, the results for each projectile were replotted as a function of  $(E_{\text{inc}} - B_a)/B_a$ , where  $B_a$  is the minimum energy required to break the projectile into two fragments and has values of 2.2, 5.5, and 19.8 MeV for deuterons,  $^3\text{He}$ , and  $\alpha$  particles, respectively. The results in Fig. 35(b) show a common trend for values of the energy ratio up to about fifteen. Above that, the points for  $^3\text{He}$  breakup keep increasing roughly linearly, and the deuteron points begin to level off.

It is possible that this difference represents a real departure from the global trend observed at lower values of  $(E_{\text{inc}} - B_a)/B_a$ , with the asymptote of the curves increasing with the mass of the projectile and thus the number of possible breakup channels. However, caution is needed, for four reasons: (1) The cross section normalization  $\mathcal{N}_{dn}$  for  $(d, n)$  breakup is unknown and was assumed to be the same as for the  $(d, p)$  channel. (2) The cross section normalization for  $(^3\text{He}, n)$  breakup is based on one very crude point and is determined only to within about a factor of two. (3) At incident energies up to around 25 MeV (energy ratio of about 3.5),  $(^3\text{He}, d)$  is the dominant  $^3\text{He}$  breakup channel, but at the higher energies, where the difference between the trends for  $d$  and  $^3\text{He}$  breakup occurs,  $(^3\text{He}, p)$  and  $(^3\text{He}, n)$  breakup together account for around 80% of the model breakup cross section. (4) For deuteron breakup, the apparent drop in the percent breakup between incident energies of 70 and 80 MeV is likely not real. The three targets used at 70 MeV [ $(E_{\text{inc}} - B_a)/B_a = 31$ ] are all heavier than the two used at 80 MeV [ $(E_{\text{inc}} - B_a)/B_a = 35$ ], and the importance of projectile breakup increases with increasing target mass.

To explore the significance of these considerations, the normalization constants for the  $(^3\text{He}, n)$  and  $(^3\text{He}, p)$  breakup channels were reduced by amounts smaller than their uncertainties. For  $(^3\text{He}, n)$ , the value was reduced from 2.0 to 1.3, and for  $(^3\text{He}, p)$ , from 4.1 to 3.9. This results in the points shown in Fig. 36, where something closer to a global trend is seen. The curve in the figure is obtained from the formula

$$f_{\text{bu}} = 0.66 \left\{ 1 - \left[ \exp \left( 0.055 \frac{E_{\text{inc}} - B_a}{B_a} \right) \right]^{-1} \right\}, \quad (33)$$

which is valid for  $E_{\text{inc}} > B_a$ . Here  $f_{\text{bu}}$  is the fraction of the total reaction cross section going into absorptive

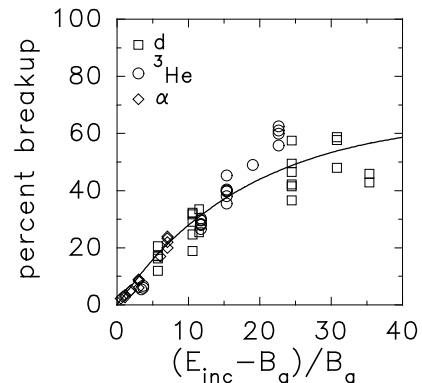


FIG. 36: Same as for Fig. 35(b) but with the cross section normalizations for the  $(^3\text{He}, n)$  and  $(^3\text{He}, p)$  breakup channels reduced as discussed in the text. The curve shows the overall trend as given by Eq. 33.

breakup. It must be emphasized that this is just a global trend to indicate the general importance of the projectile-breakup mechanism. It does not account for the variation from target to target and relies on arbitrary adjustments of poorly determined parameters.

## B. Comparison with earlier estimates

In Sect. V it was noted that different groups have deduced different dependences of the breakup cross section on target mass, depending on the continuum subtracted (if any), on the way the cross section in a particular breakup peak was determined, and even on the definition of breakup. Not surprisingly, the estimated importance of the breakup mechanism depends on the same factors. The breakup cross sections quoted in Refs. [1, 4, 7, 8, 11, 15, 17] for reactions in the current database are given only for the breakup channels measured and are either comparable to or, more often, higher than the present results. Interestingly, Ref. [15], in addition to measuring and analyzing  $(d, p)$  breakup data at 15 MeV, reanalyzed their own earlier data at 25.5 MeV [7] and arrived at breakup cross sections that are 100 to 150 mb higher than their earlier estimates. This is only about a 14% increase for  $^{181}\text{Ta}$  but a factor of 1.8 increase for  $^{27}\text{Al}$ . This underscores the sensitivity of these estimates to the analysis method.

For incident deuterons, Avrigeanu et al. [26] have used the  $(d, p)$  breakup cross section estimates from Refs. [8, 15, 17] in the current database plus isotope-ratio data from the  $^{52}\text{Cr}(d, 2n)$  reaction [19] to arrive at an empirical formulae for the elastic and total  $(d, p)$  breakup cross sections as a fraction of the total reaction cross section. The difference between these two quantities should yield the inelastic breakup or breakup-fusion cross section, which is comparable to what is here termed absorptive breakup except that some of the estimates they fit

were from theoretical calculations containing direct stripping contributions, whereas the present work does not include direct stripping. They assume that  $(d, n)$  breakup-fusion has the same cross section as  $(d, p)$  breakup fusion, similar to the assumption made here. Figure 37 shows the breakup-fusion fractions including both breakup channels from their empirical formulae compared with the absorptive breakup from the current model, which also includes the  $(d, p, d)$  cross section. For incident energies greater than  $250A^{1/3}/Z$ , their estimates have been adjusted [27] because their elastic breakup parameterization is not applicable at those energies. Their adjusted numbers are greater than the ones from this work at the lower incident energies but become comparable by around 56 MeV. In addition, they find a stronger increase of the breakup fraction with target mass at the lower incident energies. In Ref. [28], the same authors compare their breakup fraction estimates for the proton channel alone (but including elastic breakup) with the preliminary results from this project [13], where the breakup cross section that is lost in the present estimates due to the forward-angle dip was not subtracted. If that cross section is added to the present estimates for all channels, the points in the lower panel of Fig. 37 that are above a ratio of 2.0 take on values of 1.5 to 1.7 (similar to the level of agreement shown in their Fig. 4 for the proton channel), indicating a similar dependence on target mass for the two formulations, but the general discrepancy with incident energy would remain. The various estimates agree that the importance of  $(d, p)$  breakup increases with the target mass, but that dependence is here shown to be moderated by the forward-angle dip.

For the  $\alpha$ -particle breakup measured in Ref. [4], a comparison can be made on a channel-by-channel basis between the authors' estimates of the breakup cross section and those resulting from the current model. Their cross-section estimates for triton and  $^3\text{He}$  fragments are comparable to the current ones at incident energies of both 80 and 160 MeV, while their estimates for protons are a factor of six to eight higher at 80 MeV and three to five higher at 160 MeV. The theoretical curves they integrate have a high-energy tail and are normalized to the data in a way that includes much of what is here regarded as continuum cross section. The case for deuterons is intermediate, with their cross section estimates a factor of 1.5 to 2.5 higher, again largely because their theoretical curves were normalized to the data without subtracting a continuum background.

These comparisons confirm that estimates of the importance of projectile breakup obtained from the same data may vary dramatically with the analysis method and the definition of projectile breakup. However, there is agreement that this is an important reaction mechanism to consider, even for the tightly bound  $\alpha$ -particle, if the incident energy is far enough above the energy required to break the projectile into fragments. The estimates of absorptive breakup obtained in the present global analysis appear to be, if anything, on the conservative side,

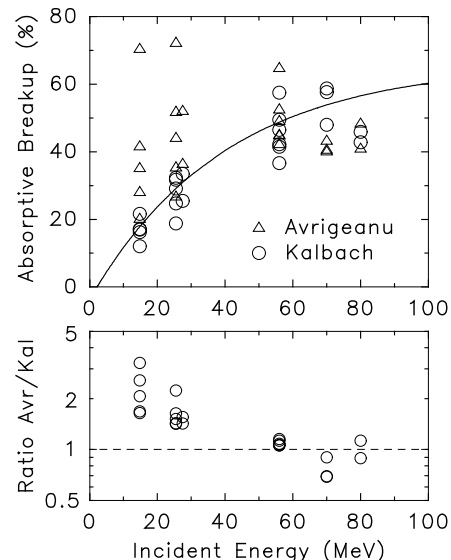


FIG. 37: Comparison of the percent of breakup-fusion. from Avrigeanu *et al.* [26, 27] with the percent of absorptive breakup found in the present work. All breakup channels are included. The upper panel shows the percentages and the lower panel gives their ratios. The curve is given by Eq. (33).

and yet as much as 50% to 60% of the reaction cross section can go into absorptive projectile breakup.

## X. SUMMARY AND CONCLUSIONS

Working from simple physical concepts and a broad database from the literature, a phenomenological model of light-projectile breakup has been developed. The model accounts for the gross features of the mechanism and is suitable for inclusion in preequilibrium reaction model codes, where it will help resolve the open question of the initial particle-hole configuration in the exciton preequilibrium model for complex projectiles with  $A = 2$  to 4. The resulting reaction codes will then yield better descriptions of the continuum underlying the breakup peaks in the data at very forward angles, thus facilitating refinements in the breakup model.

This work has also yielded useful physical insights into the breakup mechanism, generally confirming results of previous work that used more restricted data sets. The energies of the breakup peaks clearly suggest that the dominant mechanism is absorptive breakup, where the undetected projectile fragment is absorbed by the target nucleus, at least briefly, and the interaction between that fragment and the target supplies the projectile's dissociation energy. This observation is significant given the variety of assumptions (discussed in Sect. IIIB) made in theoretical formulations of projectile breakup where only one fragment is emitted. A second peak appearing in the  $(\alpha, xd)$  spectra has the energy, peak shape, and

angular distribution of the breakup peak for a proton fragment and probably results from a nucleon fragment (either a proton or a neutron) picking up a complementary nucleon from the target as it leaves. Indications of similar peaks are seen in the spectra for the ( $^3\text{He},xd$ ) reaction and are assumed to occur for incident tritons and deuterons as well. For a projectile of type  $a$ , this process is designated as  $(a,p,d)$  breakup.

The description of the breakup mechanism has the following features: (1) The energy of the breakup peak is given by the detected fragment's share of the projectile energy, corrected for Coulomb deceleration in the entrance channel of the reaction and Coulomb acceleration in the exit channel. (2) The peak widths follow fairly simple systematics that are modified when the breakup peak is narrowed due to either the kinematic limit on the ejectile's energy or the exit-channel Coulomb barrier. (3) The angular distributions are found to be exponential decays in the laboratory emission angle  $\theta$  rather than in  $\cos\theta_{\text{cm}}$ , as is the case for most preequilibrium reactions. This behavior is modified at extreme forward angles by a dip, whose size is determined by the relative sizes of the Coulomb barrier and the projectile energy. (4) The total breakup cross section for a given breakup channel and incident energy is found to vary roughly as  $(D_0)^2$  for the normal breakup peaks and as  $D_0$  for the  $(a,p,d)$  peaks, where  $D_0$  is the effective target-projectile separation distance at the point of interaction. The cross section can be reduced from this estimate by the forward-angle dip or by the exit-channel Coulomb barrier. (5) Each breakup channel has an energy barrier, related to the number of nucleons in the unobserved fragment. Above the barrier region, the cross sections display a similar, slow exponential increase with incident energy.

In the model, the double differential cross section in the  $(a,b)$  breakup channel for normal absorptive breakup, yielding an observed fragment with approximately its share of the projectile's energy, is

$$\frac{d^2\sigma_{\text{ab}}(E,\theta)}{dE d\Omega} = \sigma_{\text{ab}}(E,\theta) \frac{P_{\text{E}}^{(\text{ab})}(E)}{\int P_{\text{E}}^{(\text{ab})}(E) dE} P_{\theta}^{(\text{ab})}(\theta) \quad (34)$$

where  $\sigma_{\text{ab}}$  is given by Eq. (29),  $P_{\text{E}}(E)$  is given by Eq. (10) and  $P_{\theta}(\theta)$  is given by Eq. (26). The integral over  $P_{\text{E}}(E)$  is needed because  $P_{\text{E}}$  is not normalized when the

exit channel Coulomb barrier distorts the breakup peak. Both  $P_{\text{E}}$  and  $P_{\theta}$  depend on the specific breakup channel  $(a,b)$  and the incident energy. Similarly, for the  $(a,p,d)$  process the double differential cross section is

$$\frac{d^2\sigma_{\text{apd}}(E,\theta)}{dE d\Omega} = \sigma_{\text{apd}}(E,\theta) \frac{P_{\text{E}}^{(\text{ap})}(E)}{\int P_{\text{E}}^{(\text{ap})}(E) dE} P_{\theta}^{(\text{ap})}(\theta) \quad (35)$$

where  $\sigma_{\text{apd}}$  is given by Eq. (32) and where  $P_{\text{E}}$  and  $P_{\theta}$  are evaluated for the proton breakup fragment for the same projectile, target, and incident energy.

A major strength of this work is that a consistent method has been used to extract estimated breakup peaks from a broad range of data for three light-ion projectiles and all charged-particle breakup fragments while subtracting a reasonable underlying continuum. The resulting coherent, global description of projectile breakup should have a wider range of applicability than models developed from a more restricted database. Though still preliminary, it is expected to be a useful tool for applied work and a guide for theoretical work.

The present results confirm and underline the importance of including projectile breakup in preequilibrium reaction codes that are used for projectiles with mass numbers between two and four. For mass-two and mass-three projectiles at commonly considered incident energies, projectile breakup can account for around half of the total reaction cross section. With absorptive breakup indicated as the primary mechanism, the implication is that a large fraction of the equilibration processes in the target nuclei will be initiated not by the projectile with its full energy but by the absorbed fragment carrying its share of the projectile energy—an important effect, indeed, to consider.

## XI. ACKNOWLEDGEMENTS

This work was performed at the Triangle Universities Nuclear Laboratory under U.S. Department of Energy Grant No. DE-FG-02-97ER41033. The author is grateful to Arjan Koning for helpful comments and feedback during various phases of this work.

- 
- [1] N. Matsuoka, A. Shimizu, K. Hosono, T. Saito, M. Kondo, H. Sakaguchi, Y. Toba, A. Goto, and F. Ohtani, Nucl. Phys., **A311**, 173 (1978).
  - [2] A. Djalois, J. Bojowald, S. Gopal, W. Oelert, N. G. Puttaswamy, P. Turek, and C. Mayer-Böricke, Phys. Rev. C, **27**, 2389 (1983).
  - [3] J. R. Wu, C. C. Chang, and H. D. Holmgren, Phys. Rev. Lett., **40**, 1013 (1978).
  - [4] J. R. Wu, C. C. Chang, H. D. Holmgren, and R. W. Koontz, Phys. Rev. C, **20**, 1284 (1979).
  - [5] R. Serber, Phys. Rev. **72**, 1008 (1947).
  - [6] E. W. Hamburger, B. L. Cohen, and R. E. Price, Phys. Rev., **121**, 1143 (1961).
  - [7] J. Pampus, J. Bisplinghoff, J. Ernst, T. Mayer-Kuckuk, J. Rama Rao, G. Baur, F. Rösel, and D. Trautman, Nucl. Phys., **A311**, 141 (1978).
  - [8] N. Matsuoka, M. Kondo, A. Shimizu, T. Saito, and S. Nagamachi, Nucl. Phys., **A345**, 1 (1980).
  - [9] R. J. de Meijer and R. Kamermans, Rev. Mod. Phys., **57**, 147 (1985).

- [10] X.-H. Li, T. Udagawa, and T. Tamura, *Phys. Lett. B*, **174**, 1 (1986).
- [11] B.V. Carlson, R. Capote, and M. Sin, *Few-Body Syst.*, **57**, 307 (2016).
- [12] Angela Bonaccorso, *Physica Scripta*, **T152**, 014019 (2013).
- [13] R.A. Forrest *et al.*, “FENDL-3 Library, Final Report of the Coordinated Research Project on Nuclear Data Libraries for Advanced Systems: Fusion Devices,” IAEA report INDC(NDS)-0645, Vienna, Austria, 2013. Available at <https://www-nds.iaea.org/publications/indc/indc-nds-0645/>.
- [14] Arjan Koning, Stephan Hilaire, and Stephane Goriely, “TALYS: A Nuclear Reaction Program, User Manual,” December 2015, downloaded from <http://www.talys.eu/fileadmin/talys/user/docs/talys1.8.pdf> on 18 March 2016.
- [15] J. Kleinfeller, J. Bisplinghoff, J. Ernst, T Mayer-Kuckuk, G. Baur, B. Hoffmann, R. Shyam, F. Rösler, and D. Trautman, *Nucl. Phys.*, **A370**, 205 (1981).
- [16] A. Chevarier, N. Chevarier, A. Demeyer, A. Alevra, I. R. Lukas, M. T. Magda, and M. E. Nistor, *Nucl. Phys.*, **A237**, 354 (1975).
- [17] J. R. Wu, C. C. Chang, and H. D. Holmgren, *Phys. Rev. C*, **19**, 370 (1979).
- [18] R. W. Koontz, C. C. Chang, H. D. Holmgren, and J. R. Wu, *Phys. Rev. Lett.*, **43**, 1862 (1979).
- [19] M. G. Mustafa, T. Tamura, and T. Udagawa, *Phys. Rev. C*, **35**, 2077 (1987).
- [20] C. Kalbach, *Phys. Rev. C*, **37**, 2350 (1988)
- [21] S. Gopal, A. Djaloeis, J. Bojowald, O. Bousshid, W. Oelert, N. G. Puttaswamy, P. Turek, and C. Mayer-Böricke, *Phys. Rev. C*, **23**, 2459 (1981).
- [22] E. H. Aarts, R. K. Bhowmik, R. J. de Meijer, and S. Y. van der Werf, *Phys. Lett.*, **102B**, 307 (1981).
- [23] A. Chevarier, N. Chevarier, A. Demeyer, A. Alevra, R. Dumitrescu, I.R. Lukas, M.T. Magda, M.E. Nistor, *Nucl. Phys.*, **A231**, 64 (1974).
- [24] A. M. Kalend, B. D. Anderson, A. R. Baldwin, R. Madey, J. W. Watson, C. C. Chang, H. D. Holmgren, R. W. Koontz, J. R. Wu, and H. Machner, *Phys. Rev. C* **28**, 105 (1983).
- [25] C. Kalbach Walker, *Users Manual for PRECO-2006: Exciton Model Preequilibrium Nuclear Reaction Code with Direct Reactions*, Unpublished report from Triangle Universities Nuclear Laboratory, Duke University (February 2007); available from <http://www.nndc.bnl.gov/nndcscr/model-codes/preco-2006/>.
- [26] M. Avrigeanu, W. von Oertzen, R. A. Forrest, A. C. Obreja, F. L. Roman, V. Avrigeanu, *Fusion Eng. Design*, **84**, 418 (2009).
- [27] M. Avrigeanu, V. Avrigeanu, and C. Costache, *Euro. Phys. J. Web of Conferences*, “Proceedings of Conference on Nuclear Data for Science and Technology, ND2016,” to be published.
- [28] M. Avrigeanu, V. Avrigeanu, P. Bem, U. Fischer, M. Honusek, K. Katovsky, C. Manaiescu, J. Mrazek, E. Simeckova, and L. Zavorka, *Phys. Rev. C*, **89**, 044613 (2014) (See Fig. 4).